

See discussions, stats, and author profiles for this publication at: <https://www.researchgate.net/publication/11423378>

Functional Mimic of Dioxygen-Activating Centers in Non-Heme Diiron Enzymes: Mechanistic Implications of Paramagnetic Intermediates in the Reactions between Diiron(II) Complexes and...

ARTICLE *in* JOURNAL OF THE AMERICAN CHEMICAL SOCIETY · MAY 2002

Impact Factor: 12.11 · DOI: 10.1021/ja012251t · Source: PubMed

CITATIONS

46

READS

27

6 AUTHORS, INCLUDING:



Brad S Pierce

University of Texas at Arlington

24 PUBLICATIONS 360 CITATIONS

SEE PROFILE

Functional Mimic of Dioxygen-Activating Centers in Non-Heme Diiron Enzymes: Mechanistic Implications of Paramagnetic Intermediates in the Reactions between Diiron(II) Complexes and Dioxygen

Dongwhan Lee,[†] Brad Pierce,[‡] Carsten Krebs,[§] Michael P. Hendrich,^{*,‡}
Boi Hanh Huynh,^{*,§} and Stephen J. Lippard^{*,†}

Contribution from the Department of Chemistry, Massachusetts Institute of Technology, Cambridge, Massachusetts 02139, Department of Chemistry, Carnegie Mellon University, Pittsburgh, Pennsylvania 15213, and Department of Physics, Emory University, Atlanta, Georgia 30322

Received September 27, 2001

Abstract: Two tetracarboxylate diiron(II) complexes, $[\text{Fe}_2(\mu\text{-O}_2\text{CAr}^{\text{Tol}})_2(\text{O}_2\text{CAr}^{\text{Tol}})_2(\text{C}_5\text{H}_5\text{N})_2]$ (**1a**) and $[\text{Fe}_2(\mu\text{-O}_2\text{CAr}^{\text{Tol}})_4(4\text{-}^i\text{BuC}_5\text{H}_4\text{N})_2]$ (**2a**), where $\text{Ar}^{\text{Tol}}\text{CO}_2^- = 2,6\text{-di}(p\text{-tolyl})\text{benzoate}$, react with O_2 in CH_2Cl_2 at -78°C to afford dark green intermediates **1b** ($\lambda_{\text{max}} \cong 660\text{ nm}$; $\epsilon = 1600\text{ M}^{-1}\text{ cm}^{-1}$) and **2b** ($\lambda_{\text{max}} \cong 670\text{ nm}$; $\epsilon = 1700\text{ M}^{-1}\text{ cm}^{-1}$), respectively. Upon warming to room temperature, the solutions turn yellow, ultimately converting to isolable diiron(III) compounds $[\text{Fe}_2(\mu\text{-OH})_2(\mu\text{-O}_2\text{CAr}^{\text{Tol}})_2(\text{O}_2\text{CAr}^{\text{Tol}})_2\text{L}_2]$ ($\text{L} = \text{C}_5\text{H}_5\text{N}$ (**1c**), $4\text{-}^i\text{BuC}_5\text{H}_4\text{N}$ (**2c**)). EPR and Mössbauer spectroscopic studies revealed the presence of equimolar amounts of valence-delocalized $\text{Fe}^{\text{II}}\text{Fe}^{\text{III}}$ and valence-trapped $\text{Fe}^{\text{III}}\text{Fe}^{\text{IV}}$ species as major components of solution **2b**. The spectroscopic and reactivity properties of the $\text{Fe}^{\text{III}}\text{Fe}^{\text{IV}}$ species are similar to those of the intermediate X in the RNR–R2 catalytic cycle. EPR kinetic studies revealed that the processes leading to the formation of these two distinctive paramagnetic components are coupled to one another. A mechanism for this reaction is proposed and compared with those of other synthetic and biological systems, in which electron transfer occurs from a low-valent starting material to putative high-valent dioxygen adduct(s).

Introduction

Structural modules comprising two iron atoms ligated by four carboxylate and two imidazole residues occur in selected non-heme diiron enzymes that activate dioxygen.¹ The hydroxylase component of methane monooxygenase (MMOH),^{2,3} the R2 component of ribonucleotide reductase (RNR–R2),^{4,5} and stearoyl–acyl carrier protein (ACP) Δ^9 -desaturase ($\Delta 9\text{D}$)^{6,7} are representative of such metalloenzymes, in which coordinatively

unsaturated dimetallic centers are used to harness the oxidizing power of dioxygen. In the enzyme reaction cycles, highly reactive intermediates are accessed through controlled delivery of reducing equivalents to the metal-bound O_2 -derived ligands. Notable functional features of this enzyme family include the evolution of distinctive higher oxidation state intermediates from essentially identical initial dioxygen adducts (Scheme 1). Current information points toward the involvement of high-valent iron(IV) species in C–H activation by MMOH and tyrosine oxidation by RNR–R2. The mechanism(s) by which reductive activation of an O–O bond affords reactive iron–oxo units, however, is not fully understood. Specifically, two-electron reduction of the peroxide ligand by iron in (peroxo)diiron(III) species affords an $\text{Fe}^{\text{IV}}\text{Fe}^{\text{IV}}$ center in MMOH_0 ,^{8–10} whereas delivery of one external electron is required for a conversion to the $\text{Fe}^{\text{III}}\text{Fe}^{\text{IV}}$ core in RNR–R2 X.¹¹ The fate of these O_2 -derived intermediates might be affected by carboxylate shifts,¹² the functional relevance of which needs to be elucidated in conjunction with the dynamic core conversions implicated in the catalytic cycle.²

[†] Massachusetts Institute of Technology.

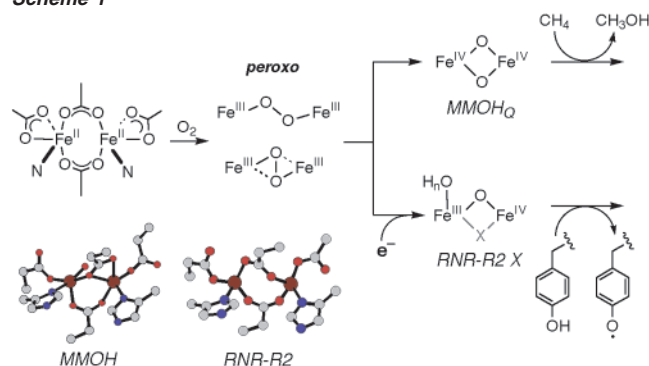
[‡] Carnegie Mellon University.

[§] Emory University.

- (1) (a) Feig, A. L.; Lippard, S. J. *Chem. Rev.* **1994**, *94*, 759–805. (b) Wallar, B. J.; Lipscomb, J. D. *Chem. Rev.* **1996**, *96*, 2625–2657. (c) Que, L., Jr.; Dong, Y. *Acc. Chem. Res.* **1996**, *29*, 190–196. (d) Lange, S. J.; Que, L., Jr. *Curr. Opin. Chem. Biol.* **1998**, *2*, 159–172. (e) Stahl, S. S.; Lippard, S. J. In *Iron Metabolism: Inorganic Biochemistry and Regulatory Mechanisms*; Ferreira, G. C.; Moura, J. J. G.; Franco, R., Eds.; Wiley-VCH: Weinheim, Germany, 1999; pp 303–321. (f) Du Bois, J.; Mizoguchi, T. J.; Lippard, S. J. *Coord. Chem. Rev.* **2000**, *200*–202, 443–485. (g) Solomon, E. I.; Brunold, T. C.; Davis, M. I.; Kemsley, J. N.; Lee, S.-K.; Lehnert, N.; Neese, F.; Skulan, A. J.; Yang, Y.-S.; Zhou, J. *Chem. Rev.* **2000**, *100*, 235–349.
- (2) Merckx, M.; Kopp, D. A.; Sazinsky, M. H.; Blazyk, J. L.; Müller, J.; Lippard, S. J. *Angew. Chem., Int. Ed. Engl.* **2001**, *40*, 2782–2807.
- (3) Whittington, D. A.; Lippard, S. J. In *Handbook of Metalloproteins*; Messerschmidt, A.; Huber, R.; Poulos, T.; Wieghardt, K., Eds.; John Wiley & Sons: Chichester, U.K., 2001; pp 712–724.
- (4) Logan, D. T.; Su, X.-D.; Åberg, A.; Regnström, K.; Hajdu, J.; Eklund, H.; Nordlund, P. *Structure* **1996**, *4*, 1053–1064.
- (5) Stubbe, J.; van der Donk, W. A. *Chem. Rev.* **1998**, *98*, 705–762.
- (6) Lindqvist, Y.; Huang, W.; Schneider, G.; Shanklin, J. *EMBO J.* **1996**, *15*, 4081–4092.
- (7) Yang, Y.-S.; Broadwater, J. A.; Pulver, S. C.; Fox, B. G.; Solomon, E. I. *J. Am. Chem. Soc.* **1999**, *121*, 2770–2783.

- (8) Lee, S.-K.; Fox, B. G.; Froland, W. A.; Lipscomb, J. D.; Münck, E. *J. Am. Chem. Soc.* **1993**, *115*, 6450–6451.
- (9) Liu, K. E.; Valentine, A. M.; Wang, D.; Huynh, B. H.; Edmondson, D. E.; Salifoglou, A.; Lippard, S. J. *J. Am. Chem. Soc.* **1995**, *117*, 10174–10185.
- (10) Shu, L.; Nesheim, J. C.; Kauffmann, K.; Münck, E.; Lipscomb, J. D.; Que, L., Jr. *Science* **1997**, *275*, 515–518.

Scheme 1



Well-defined synthetic analogues having chemical properties comparable to those of non-heme diiron enzymes have complemented our understanding of biological dioxygen activation.^{1c,f,13–15} Several examples are now available in which reactions between diiron(II) complexes and O₂ afford (peroxo)-diiron(III) species (Table S1),^{16–22} the mechanisms of formation and decay of which have been investigated by kinetic techniques.^{20,22–26} A few (peroxo)diiron(III) complexes have been isolated at low temperatures and structurally characterized,^{16b,17c,18} providing insights into the geometric and electronic structures of the transient enzyme intermediates.^{1g,27–31} High-valent di-(μ-oxo)iron(III)iron(IV) complexes were prepared by reactions

between diiron(III) complexes and H₂O₂ and studied as spectroscopic and structural models for RNR–R2 X.³² Related Fe^{III}Fe^{IV} species were accessed by one-electron chemical oxidation of a di(μ-oxo)diiron(III) precursor³³ or by reactions between a diiron(II) precursor and O₂ at low temperatures.²² Most of the model compounds investigated so far, however, are built on polyamine/imine donor ligands, a coordination environment significantly different from those of the carboxylate-rich active sites in MMOH and RNR–R2. Integrating a parallel functional chemistry into a well-defined structural replica of the non-heme diiron enzymes is a long-standing problem in bioinorganic chemistry, the solution to which would provide significant insights into the underlying chemical principles of enzyme action.

Recently, we reported that tetracarboxylate diiron(II) complexes [Fe₂(μ-O₂CAr^{Tol})₂(O₂CAr^{Tol})₂(C₅H₅N)₂] (**1a**) or [Fe₂(μ-O₂CAr^{Tol})₄(4-^tBuC₅H₄N)₂] (**2a**), where Ar^{Tol}CO₂[–] = 2,6-di-(*p*-tolyl)benzoate, react with dioxygen in CH₂Cl₂ at –78 °C to afford thermally sensitive intermediates having broad intense visible absorptions at 660–670 nm.^{34,35} EPR and Mössbauer data were consistent with the existence of an equimolar amount of Fe^{II}Fe^{III} and Fe^{III}Fe^{IV} species as major components of these intermediates.³⁵ A mechanism for this unprecedented process was proposed (eq 1), based solely on the observed reaction stoichiometry.



In this paper, we present a full description of the reactions of **1a** and **2a** with dioxygen. Spectroscopic and reactivity properties of the metastable reaction intermediates are described and compared with those of independently synthesized mixed-valence compounds. Mechanistic implications of this novel transformation are discussed and compared with other synthetic and biological systems, highlighting the importance of regulated electron trafficking in reductive activation of dioxygen.

Experimental Section

General Considerations. All reagents were obtained from commercial suppliers and used as received unless otherwise noted. Dichloromethane was distilled over CaH₂ under nitrogen. Diethyl ether, pentanes, and tetrahydrofuran (THF) were saturated with nitrogen and purified by passage through activated Al₂O₃ columns under nitrogen.³⁶ The compounds [H(OEt₂)₂](BAR⁴)₃^{37,38} and 3,3',5,5'-tetra-*tert*-butyl-1,1'-bi-2,2'-phenol³⁹ were synthesized according to literature procedures. Syntheses of the compounds [Fe₂(μ-O₂CAr^{Tol})₂(O₂CAr^{Tol})₂(C₅H₅N)₂] (**1a**),³⁴ [Fe₂(μ-O₂CAr^{Tol})₄(4-^tBuC₅H₄N)₂] (**2a**),³⁵ [Fe₂(μ-OH)₂(μ-O₂CAr^{Tol})₂(O₂CAr^{Tol})₂(C₅H₅N)₂] (**1c**),³⁴ [Fe₂(μ-OH)₂(μ-O₂CAr^{Tol})₂

- (11) (a) Ravi, N.; Bollinger, J. M., Jr.; Huynh, B. H.; Edmondson, D. E.; Stubbe, J. *J. Am. Chem. Soc.* **1994**, *116*, 8007–8014. (b) Bollinger, J. M., Jr.; Tong, W. H.; Ravi, N.; Huynh, B. H.; Edmondson, D. E.; Stubbe, J. *J. Am. Chem. Soc.* **1994**, *116*, 8015–8023. (c) Sturgeon, B. E.; Burdi, D.; Chen, S.; Huynh, B. H.; Edmondson, D. E.; Stubbe, J.; Hoffman, B. M. *J. Am. Chem. Soc.* **1996**, *118*, 7551–7557. (d) Burdi, D.; Sturgeon, B. E.; Tong, W. H.; Stubbe, J.; Hoffman, B. M. *J. Am. Chem. Soc.* **1996**, *118*, 281–282. (e) Willems, J.-P.; Lee, H.-I.; Burdi, D.; Doan, P. E.; Stubbe, J.; Hoffman, B. M. *J. Am. Chem. Soc.* **1997**, *119*, 9816–9824. (f) Burdi, D.; Willems, J.-P.; Riggs-Gelasco, P.; Antholine, W. E.; Stubbe, J.; Hoffman, B. M. *J. Am. Chem. Soc.* **1998**, *120*, 12910–12919.
- (12) Rardin, R. L.; Tolman, W. B.; Lippard, S. J. *New J. Chem.* **1991**, *15*, 417–430.
- (13) Que, L., Jr. *J. Chem. Soc., Dalton Trans.* **1997**, 3933–3940.
- (14) Westerheide, L.; Pascaly, M.; Krebs, B. *Curr. Opin. Chem. Biol.* **2000**, *4*, 235–241.
- (15) Tolman, W. B.; Spencer, D. J. E. *Curr. Opin. Chem. Biol.* **2001**, *5*, 188–195.
- (16) (a) Kitajima, N.; Tamura, N.; Amagai, H.; Fukui, H.; Moro-oka, Y.; Mizutani, Y.; Kitagawa, T.; Mathur, R.; Heerwegh, K.; Reed, C. A.; Randall, C. R.; Que, L., Jr.; Tatsumi, K. *J. Am. Chem. Soc.* **1994**, *116*, 9071–9085. (b) Kim, K.; Lippard, S. J. *J. Am. Chem. Soc.* **1996**, *118*, 4914–4915.
- (17) (a) Ménage, S.; Brennan, B. A.; Juarez-Garcia, C.; Münck, E.; Que, L., Jr. *J. Am. Chem. Soc.* **1990**, *112*, 6423–6425. (b) Dong, Y.; Ménage, S.; Brennan, B. A.; Elgren, T. E.; Jang, H. G.; Pearce, L. L.; Que, L., Jr. *J. Am. Chem. Soc.* **1993**, *115*, 1851–1859. (c) Dong, Y.; Yan, S.; Young, V. G., Jr.; Que, L., Jr. *Angew. Chem., Int. Ed. Engl.* **1996**, *35*, 618–620.
- (18) Ookubo, T.; Sugimoto, H.; Nagayama, T.; Masuda, H.; Sato, T.; Tanaka, K.; Maeda, Y.; Okawa, H.; Hayashi, Y.; Uehara, A.; Suzuki, M. *J. Am. Chem. Soc.* **1996**, *118*, 701–702.
- (19) Dong, Y.; Zang, Y.; Shu, L.; Wilkinson, E. C.; Que, L., Jr. *J. Am. Chem. Soc.* **1997**, *119*, 12683–12684.
- (20) LeCloux, D. D.; Barrios, A. M.; Mizoguchi, T. J.; Lippard, S. J. *J. Am. Chem. Soc.* **1998**, *120*, 9001–9014.
- (21) Hagadorn, J. R.; Que, L., Jr.; Tolman, W. B. *J. Am. Chem. Soc.* **1998**, *120*, 13531–13532.
- (22) MacMurdo, V. L.; Zheng, H.; Que, L., Jr. *Inorg. Chem.* **2000**, *39*, 2254–2255.
- (23) Feig, A. L.; Lippard, S. J. *J. Am. Chem. Soc.* **1994**, *116*, 8410–8411.
- (24) Feig, A. L.; Becker, M.; Schindler, S.; van Eldik, R.; Lippard, S. J. *Inorg. Chem.* **1996**, *35*, 2590–2601.
- (25) Feig, A. L.; Masschelein, A.; Bakac, A.; Lippard, S. J. *J. Am. Chem. Soc.* **1997**, *119*, 334–342.
- (26) Kryatov, S. V.; Rybak-Akimova, E. V.; MacMurdo, V. L.; Que, L., Jr. *Inorg. Chem.* **2001**, *40*, 2220–2228.
- (27) Valentine, A. M.; Stahl, S. S.; Lippard, S. J. *J. Am. Chem. Soc.* **1999**, *121*, 3876–3887.
- (28) Lee, S.-K.; Lipscomb, J. D. *Biochemistry* **1999**, *38*, 4423–4432.
- (29) Bollinger, J. M., Jr.; Krebs, C.; Vicol, A.; Chen, S.; Ley, B. A.; Edmondson, D. E.; Huynh, B. H. *J. Am. Chem. Soc.* **1998**, *120*, 1094–1095.
- (30) Broadwater, J. A.; Ai, J.; Loehr, T. M.; Sanders-Loehr, J.; Fox, B. G. *Biochemistry* **1998**, *37*, 14664–14671.

- (31) Brunold, T. C.; Tamura, N.; Kitajima, N.; Moro-oka, Y.; Solomon, E. I. *J. Am. Chem. Soc.* **1998**, *120*, 5674–5690.
- (32) (a) Dong, Y.; Fujii, H.; Hendrich, M. P.; Leising, R. A.; Pan, G.; Randall, C. R.; Wilkinson, E. C.; Zang, Y.; Que, L., Jr.; Fox, B. G.; Kauffmann, K.; Münck, E. *J. Am. Chem. Soc.* **1995**, *117*, 2778–2792. (b) Dong, Y.; Que, L., Jr.; Kauffmann, K.; Münck, E. *J. Am. Chem. Soc.* **1995**, *117*, 11377–11378. (c) Hsu, H.-F.; Dong, Y.; Shu, L.; Young, V. G., Jr.; Que, L., Jr. *J. Am. Chem. Soc.* **1999**, *121*, 5230–5237.
- (33) Zheng, H.; Yoo, S. J.; Münck, E.; Que, L., Jr. *J. Am. Chem. Soc.* **2000**, *122*, 3789–3790.
- (34) Lee, D.; Lippard, S. J. *J. Am. Chem. Soc.* **1998**, *120*, 12153–12154.
- (35) Lee, D.; Du Bois, J.; Petasis, D.; Hendrich, M. P.; Krebs, C.; Huynh, B. H.; Lippard, S. J. *J. Am. Chem. Soc.* **1999**, *121*, 9893–9894.
- (36) Pangborn, A. B.; Giardello, M. A.; Grubbs, R. H.; Rosen, R. K.; Timmers, F. J. *Organometallics* **1996**, *15*, 1518–1520.

(O₂CAr^{Tol})₂(4-^tBuC₅H₄N)₂] (**2c**),³⁵ [Fe₂(μ-O₂CAr^{Tol})₄(C₅H₅N)₂](OTf) (**1mv**), and [Fe₂(μ-O₂CAr^{Tol})₄(4-^tBuC₅H₄N)₂](PF₆) (**2mv**)⁴⁰ were reported previously. Dioxygen (99.994%, BOC Gases) was dried by passing the gas stream through a column of Drierite. ¹⁸O-enriched dioxygen (99%) was supplied by ICON, NY. All air-sensitive manipulations were carried out under nitrogen in a Vacuum Atmospheres drybox or by standard Schlenk line techniques. Manometric experiments were performed according to a literature procedure,^{41a} with [IrCl(CO)(PPh₃)₂] as a standard.

Oxygenation of 1a and 2a. In a typical reaction, compound **1a** or **2a** was dissolved in freshly distilled CH₂Cl₂ and loaded into a vessel fitted with a rubber septum. The solution was cooled to -78 °C in a dry ice/acetone bath. Dioxygen was bubbled directly into the solution, resulting in a color change from yellow to dark emerald green, indicating the formation of **1b** or **2b**.

X-ray Crystallographic Studies. Intensity data were collected on a Bruker (formerly Siemens) CCD diffractometer with graphite-monochromated Mo Kα radiation (λ = 0.710 73 Å), controlled by a Pentium-based PC running the SMART software package.⁴² Single crystals were mounted at room temperature on the tips of quartz fibers, coated with Paratone-N oil, and cooled to 188 K under a stream of cold nitrogen maintained by a Bruker LT-2A nitrogen cryostat. Data collection and reduction protocols are described elsewhere.⁴³ The structures were solved by direct methods and refined on F² by using the SHELXTL software package.⁴⁴ Empirical absorption corrections were applied with SADABS,⁴⁵ part of the SHELXTL program package, and the structures were checked for higher symmetry by the program PLATON.⁴⁶ All non-hydrogen atoms were refined anisotropically unless otherwise noted. Hydrogen atoms were assigned idealized positions and given thermal parameters equivalent to either 1.5 (methyl hydrogen atoms) or 1.2 (all other hydrogen atoms) times the thermal parameter of the carbon atom to which they were attached. The disordered *tert*-butyl group on 4-*tert*-butylpyridine in [Fe(O₂CAr^{Tol})₂(2,4-^tBu₂C₆H₃O)-(4-^tBuC₅H₄N)] is equally distributed over two positions and refined isotropically.

Physical Measurements. ¹H NMR spectra were recorded on a Varian Mercury 300 spectrometer; chemical shifts are reported versus tetramethylsilane and were referenced to the residual solvent peaks. FT-IR spectra were recorded on a Bio Rad FTS-135 instrument with Win-IR software. UV-vis spectra were recorded on a Hewlett-Packard 8452A diode array spectrophotometer. The low-temperature UV-vis

experiments were executed by using a custom-made quartz cuvette with a 1 cm path length fused into a vacuum-jacketed dewar. Low-temperature titration was monitored by using a Spectral Instruments Model 440 CCD Array UV-vis spectrophotometer in conjunction with a remote fiber-optic dip probe with a 1 cm path length.

Resonance Raman Spectroscopy. A Coherent Innova 90 Kr⁺ laser with an excitation wavelength of 647.1 nm and 50 mW of power was used to acquire Raman data. A 0.6 m single monochromator (1200 grooves/nm grating), with an entrance slit of 100 μm, and a TE-CCD-1100-PB-VISAR detector (Princeton Instruments, Inc.) cooled to -40 °C were used in a standard backscattering configuration. A holographic notch filter (Kaiser Optical Systems) was used to attenuate Rayleigh scattering. Spectra were collected in CH₂Cl₂ solution at -78 °C with the same low-temperature dewar used in UV-vis studies. Solutions were made as concentrated as possible, ~10 mM in the best cases, to ensure an optimal signal-to-noise ratio. A total of 400 scans, each with a 1 s exposure time, were typically collected for each sample. Raman shifts were calibrated with DMF as an external standard. The data were processed on a Gateway 2000 computer using WINSPEC 3.2.1 software (Princeton Instruments, Inc.).

Mössbauer Spectroscopy. Field-dependent Mössbauer spectra were acquired on a spectrometer equipped with a Janis 12 CNDT/SC SuperVaritemp cryostat and an 8 T superconducting magnet. Zero-field Mössbauer spectra were obtained at 4.2 K on an MS1 spectrometer (WEB Research Co.). The spectrometers were operated in constant acceleration mode in transmission geometry. Zero velocity of the Mössbauer spectra refers to the centroid of the room temperature spectrum of metallic Fe-foil. Solid samples of **2b** were prepared by concentrating the oxygenation product of **2a** (100 mg) in CH₂Cl₂ (3 mL) at -78 °C by using a diffusion pump operating at <10⁻⁵ mm Hg. A dark green solid material thus isolated was suspended in BN and stored at 77 K. A solid sample of **2c** was prepared by suspending ~0.02 mmol of the powdered material in Apeizon N grease and packing the mixture into a nylon sample holder. A frozen solution sample of **2c** was prepared in THF by loading 1 mL of a ~20 mM solution into a nylon sample holder and freezing it at 77 K.

The Mössbauer spectra of **2b** were analyzed by using the spin Hamiltonian (eq 2), in which *H_e* represents the electronic properties of the diiron clusters and *H_{hf}* describes the hyperfine interactions of the iron nuclei with their surrounding electrons. The electronic part, *H_e*,

$$H_S = H_e + H_{hf} \quad (2)$$

contains the zero-field and Zeeman interactions (eq 3), and *H_{hf}* contains the quadrupolar (the first summation) and magnetic (the second summation) hyperfine interactions (eq 4). All symbols have their usual meaning. The symbol *S* represents the total electronic spin of the ground

$$H_e = D \left[S_z^2 - \frac{S(S+1)}{3} \right] + \frac{E}{D} (S_x^2 - S_y^2) + \beta \mathbf{S} \cdot \mathbf{g} \cdot \mathbf{H} \quad (3)$$

$$H_{hf} = \sum_{i=1}^2 \frac{eQ(V_{zz})_i}{4} \left[I_{zi}^2 - \frac{I_i(I_i+1)}{3} + \frac{\eta}{3} (I_{xi}^2 - I_{yi}^2) \right] + \sum_{i=1}^2 (\mathbf{S} \cdot \mathbf{A}_i \cdot \mathbf{I}_i - g_n \beta_n \mathbf{H} \cdot \mathbf{I}_i) \quad (4)$$

state of the diiron clusters, and *A_i* is the magnetic hyperfine tensor describing the interaction between the total spin *S* and the individual iron nuclear spins, *I_i*. The Mössbauer spectra of **2c** were fit to Lorentzian lines by using the WMOSS plot and fit program.⁴⁷

EPR Spectroscopy. X-band (9 GHz) EPR spectra were recorded on a Bruker 300 spectrometer equipped with an Oxford ESR 910 cryostat for low-temperature measurements and a Bruker bimodal cavity

- (37) Abbreviations used: [BAr'₄]⁻, [(3,5-(CF₃)₂C₆H₃)₄B]⁻; H₂XDK, *m*-xylylenediamine bis(Kemp's triacid imide); BXDK, the benzyl derivative of XDK; dipic, 2,6-pyridinedicarboxylate; H₃dfmp, 2,6-diformyl-4-methylphenoldioxime; HPTB, anion of *N,N,N',N'*-tetraakis(2-benzimidazolylmethyl)-2-hydroxyl-1,3-diaminopropane; L¹, [2+2] condensation product of propylenediamine and 2,6-diformyl-4-methylphenol; L², *N,N'*-ethylenebis(salicylamine); L³, *N,N,N',N'*-tetramethyl-(1*R*,2*R*)-cyclohexanediamine; Me₃TACN, 1,4,7-trimethyl-1,4,7-triazacyclononane; 6-Me₃-TPA, tris(6-methyl-2-pyridylmethyl)amine; 6-Me-TPA, *N*-(6-methyl-2-pyridylmethyl)-*N,N*-bis(2-pyridylmethyl)amine; OAc⁻, acetate; Ph-bimp, 2,6-bis[bis(2-(1-methyl-4,5-diphenylimidazolyl)methyl)aminomethyl]-4-methylphenolate; PhCyCO₂H, 1-phenylcyclohexanecarboxylic acid; pz', 3,5-bis(isopropyl)pyrazolyl; H₃salmp, 2-bis(salicylideneamino)methylphenol; Ar^{Me}CO₂H, 2,6-dimesitylbenzoic acid; Ar^{4-FPh}CO₂H, 2,6-di(4-fluorophenyl)benzoic acid.
- (38) Brookhart, M.; Grant, B.; Volpe, A. F., Jr. *Organometallics* **1992**, *11*, 3920–3922.
- (39) van der Linden, A.; Schaverien, C. J.; Meijboom, N.; Ganter, C.; Orpen, A. G. *J. Am. Chem. Soc.* **1995**, *117*, 3008–3021.
- (40) Lee, D.; Krebs, C.; Huynh, B. H.; Hendrich, M. P.; Lippard, S. J. *J. Am. Chem. Soc.* **2000**, *122*, 5000–5001.
- (41) (a) Mahapatra, S.; Halfen, J. A.; Wilkinson, E. C.; Pan, G.; Wang, X.; Young, V. G., Jr.; Cramer, C. J.; Que, L., Jr.; Tolman, W. B. *J. Am. Chem. Soc.* **1996**, *118*, 11555–11574. (b) Mahapatra, S.; Halfen, J. A.; Tolman, W. B. *J. Am. Chem. Soc.* **1996**, *118*, 11575–11586.
- (42) SMART v5.05: *Software for the CCD Detector System*; Bruker AXS: Madison, WI, 1998.
- (43) Feig, A. L.; Bautista, M. T.; Lippard, S. J. *Inorg. Chem.* **1996**, *35*, 6892–6898.
- (44) Sheldrick, G. M. *SHELXTL97-2: Program for the Refinement of Crystal Structures*; University of Göttingen: Göttingen, Germany, 1997.
- (45) Sheldrick, G. M. *SADABS: Area-Detector Absorption Correction*; University of Göttingen: Göttingen, Germany, 1996.
- (46) Spek, A. L. *PLATON, A Multipurpose Crystallographic Tool*; Utrecht University: Utrecht, The Netherlands, 1998.

- (47) Kent, T. A. *WMOSS v2.5: Mössbauer Spectral Analysis Software*; WEB Research Co.: Minneapolis, MN, 1998.

for generation of the microwave fields parallel and transverse to the static field. Q-band (35 GHz) EPR spectra were recorded on a Bruker 200 spectrometer equipped with a locally built low-temperature microwave probe and cryogenic system.⁴⁸ For both instruments, the microwave frequency was calibrated by a frequency counter and the magnetic field was calibrated with an NMR gaussmeter. The Oxford thermocouple temperature was calibrated using a carbon glass resistor temperature probe (CGR-1-1000 Lake Shore Cryotronics). For X- and Q-band EPR, the magnetic field modulation was 100 kHz unless noted otherwise. All experimental data were collected under nonsaturating conditions.

EPR Simulations. Interpretation of the EPR spectra utilizes the spin Hamiltonian given in eq 3. Simulations of the EPR spectra are calculated from diagonalization of eq 3 with a locally written program. The powder pattern is generated for a uniform spherical distribution of the magnetic field vector **B**. The transition intensities are calculated from the square of the transition moment. The spectral line width is dominated by *D*-strain and simulations use distributions of the *D* and *E/D* to give the correct line widths. The distributions are specified as σ_D and $\sigma_{E/D}$.

The simulations are generated with careful consideration of all intensity factors, both theoretical and instrumental. This approach allows direct comparison of simulated spectra to the absolute intensity scale of the experimental spectrum having a known sample concentration. The only unknown factor relating the spin concentration to signal intensity is an instrumental one that depends on the microwave detection system. This factor, however, is determined by the spin standard, CuEDTA, for which the copper concentration was accurately determined from plasma emission spectroscopy.

Magnetic Susceptibility Measurements. Magnetic susceptibility data for solid samples of **1c** and **2c** were measured between 5 and 300 K with applied magnetic fields of 0.1 T using a Quantum Design MPMS SQUID susceptometer. Samples were loaded in gel capsules and suspended in plastic straws. The susceptibilities of the straw and gel capsule were independently determined at the same temperature range and field for correction of their contribution to the total measured susceptibility. Underlying diamagnetism of the sample was calculated from Pascal's constants.⁴⁹ The molar magnetic susceptibility data were fit to the expression derived from the spin-only isotropic HDvV exchange Hamiltonian $\mathcal{H} = -2JS_1 \cdot S_2$, where $S_1 = S_2 = 5/2$. This expression is given in eq 5, where $x = J/kT$. No corrections were made for TIP or paramagnetic impurities.

$$\chi_M = \frac{Ng^2\mu_B^2}{kT} \frac{2e^{2x} + 10e^{6x} + 28e^{12x} + 60e^{20x} + 110e^{30x}}{1 + 3e^{2x} + 5e^{6x} + 7e^{12x} + 9e^{20x} + 11e^{30x}} \quad (5)$$

Titration of **2b with **Cp₂Fe** or **Cp^{*}₂Fe**.** A CH₂Cl₂ solution of **2a**, typically ~0.45 mM, was cooled to -78 °C and subjected to an O₂ purge for 5 min. The development of **2b** was followed by UV-vis spectroscopy for 1 h, during which time the 670 nm absorption reached a maximum. Excess O₂ was removed by bubbling argon through the solution for >20 min. Aliquots of either Cp₂Fe or Cp^{*}₂Fe in CH₂Cl₂ were delivered to the solution under argon by using a gas-tight microsyringe. Spectral measurements were made after each addition and corrected for dilution.

EPR Kinetics. Kinetic experiments were performed in calibrated EPR tubes. A CH₂Cl₂ solution sample of **2a** (1.12 mM) was prepared in a drybox, and each 300 μL aliquot was loaded into an EPR tube fitted with a rubber septum. The samples were brought out, placed under a positive Ar pressure, and held at -78 °C. Dioxygen (2.5 mL) was bubbled through the solution over a period of 30 s by injection from a gas-tight syringe. The reactions were kept at -78 °C for varying periods of time (1–45 min) and quenched by flash-freezing the EPR tubes at 77 K. The amount of *S* = 9/2 species was determined relative

to a quantitative simulation by using the spectral parameters given in Figure 4. This value was later confirmed, to within 10% of the concentration, by a pure sample of **2mv** of known concentration. The *S* = 1/2 component was quantitated by double integration of the EPR signal.

Generation of **2b in the Presence of H⁺.** Solution samples of **2a** (1.21 mM) mixed with [H(OEt)₂](BAR⁴) (0.63 mM) were prepared in CH₂Cl₂ and loaded into calibrated EPR tubes. Oxygenation was carried out in a manner similar to that described for EPR kinetics (see above), and the reaction was quenched after incubation for 5 min. The amounts of *S* = 9/2 and *S* = 1/2 components were quantitated and compared with those of a kinetics sample quenched after an identical period of time.

Ligand Recovery. A CH₂Cl₂ (30 mL) suspension of **1a** (102 mg, 69.4 μmol) was cooled to -78 °C. Dioxygen was bubbled through the solution for 5 min, and the resulting dark emerald green solution was stirred for 0.5 h. Unreacted dioxygen was removed by bubbling Ar through the solution for 0.5 h. The solution was warmed to room temperature and quenched by adding an aqueous HCl solution (10%, 20 mL). The organic layer was separated, and the aqueous layer was extracted with 3 × 20 mL portions of CH₂Cl₂. The combined extracts were dried over MgSO₄, filtered, and concentrated under reduced pressure to afford Ar^{Tol}CO₂H as an off-white solid (79 mg, 0.261 mmol, 94% recovery yield). ¹H NMR (300 MHz, CD₂Cl₂) δ 7.52 (t, 1H), 7.35 (d, 2H), 7.31 (d, 4H), 7.22 (d, 4H), 2.41 (s, 6H); FT-IR (thin film deposited from CD₂Cl₂ solution on NaCl, cm⁻¹) 3027, 2925, 1699, 1516, 1455, 1294, 816, 803, 781. LRMS (EI): *m/z* 302 (M⁺).

Reactions of **1b with 2,4,6-Tri-*tert*-butylphenol.** A CH₂Cl₂ solution (10 mL) of **1a** (0.37 mM) was purged with dioxygen at -78 °C to afford **1b**. Excess O₂ was removed by bubbling Ar through the solution. A portion of 2,4,6-tri-*tert*-butylphenol (8.1 μmol, 2.2 equiv) in CH₂Cl₂ (30 μL) was added, and the spectral change was monitored by UV-vis spectroscopy. A similarly prepared sample of **1b** was transferred to a precooled EPR tube containing an equal volume of Ar-purged toluene. The mixture was rapidly frozen at 77 K and analyzed by X-band EPR spectroscopy. The spectra were compared with those of 2,4,6-tri-*tert*-butylphenoxyl radical generated independently by a chemical method.⁵⁰

Reaction of **2b with 2,4-Di-*tert*-butylphenol.** A CH₂Cl₂ solution (10 mL) of **2a** (204 mg, 0.129 mmol) was purged with O₂ at -78 °C to afford **2b**. The dark green solution was stirred for 2 h at -78 °C, and excess dioxygen was removed by Ar bubbling. A portion of 2,4-di-*tert*-butylphenol (55 mg, 0.27 mmol) was added as a solid. The mixture was warmed to room temperature to afford an intense blue solution. Volatile fractions were removed, and the remaining solid material was extracted into CH₂Cl₂ (25 mL). A portion of aqueous HCl (10%, 15 mL) was added, and the organic layer was separated. The aqueous layer was extracted with 4 × 25 mL portions of CH₂Cl₂. The combined extracts were dried over MgSO₄, filtered, and concentrated under reduced pressure to provide a pale yellow residue. The mixture (203 mg, 98% overall recovery yield) comprised Ar^{Tol}CO₂H, 2,4-di-*tert*-butylphenol, and 3,3',5,5'-tetra-*tert*-butyl-1,1'-bi-2,2'-phenol, as judged by comparison with the ¹H NMR spectra of authentic samples. The amount of the 2,2'-biphenol product (26 μmol, 40% based on **2a**) was determined by comparison of the integration of the methyl group peaks (1.45 and 1.33 ppm) against the methyl proton signals from the unreacted 2,4-di-*tert*-butylphenol (1.41 and 1.30 ppm).

Reaction of **2mv with 2,4-Di-*tert*-butylphenol.** To a dark green CH₂Cl₂ (10 mL) solution of **2mv** (114 mg, 65.8 μmol) was added 2,4-di-*tert*-butylphenol (58 mg, 0.28 mmol) under nitrogen. The reaction mixture was stirred for 2 h at room temperature and quenched by adding aqueous HCl (10%, 15 mL). The components in the CH₂Cl₂ layer were isolated and analyzed as described above. The mixture (124 mg, 91%

(48) Petasis, D.; Hendrich, M. P. *J. Magn. Reson.* **1999**, *136*, 200–206.

(49) Carlin, R. L. *Magnetochemistry*; Springer-Verlag: New York, 1986.

(50) Goldberg, D. P.; Koulougliotis, D.; Brudvig, G. W.; Lippard, S. J. *J. Am. Chem. Soc.* **1995**, *117*, 3134–3144.

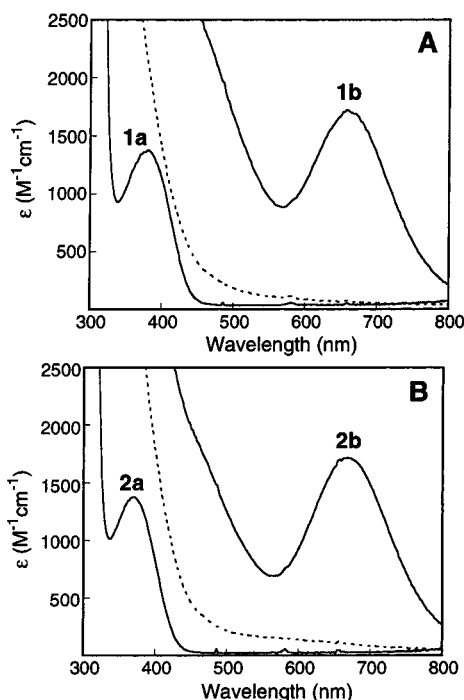


Figure 1. Electronic absorption spectra for the formation of dioxygen adducts of diiron(II) complexes in CH₂Cl₂ at −78 °C and their thermal decay products (---): (A) [Fe₂(μ-O₂CAr^{Tol})₂(O₂CAr^{Tol})₂(C₅H₅N)₂] (**1a**); (B) [Fe₂(μ-O₂CAr^{Tol})₄(4-*t*BuC₅H₄N)₂] (**2a**).

overall recovery yield) was composed of Ar^{Tol}CO₂H and unreacted 2,4-di-*tert*-butylphenol, as judged by comparison with the ¹H NMR spectra of authentic samples. No coupling product, 3,3',5,5'-tetra-*tert*-butyl-1,1'-bi-2,2'-phenol, was detected.

Results

Reactions of Diiron(II) Complexes [Fe₂(μ-O₂CAr^{Tol})₂(O₂CAr^{Tol})₂(C₅H₅N)₂] (**1a**) and [Fe₂(μ-O₂CAr^{Tol})₄(4-*t*BuC₅H₄N)₂] (**2a**) with O₂. (a) **UV–Vis Spectroscopy.** Oxygenation of a CH₂Cl₂ solution of **1a** at −78 °C resulted in the formation of a deep green species **1b** with a broad ($\nu_{1/2} \approx 3700$ cm^{−1}) visible absorption centered at ~660 nm ($\tilde{\nu} \approx 15\,200$ cm^{−1}; $\epsilon = 1600$ M^{−1} cm^{−1}) (Figure 1A). Since **1a** cannot be regenerated from **1b** by evacuation or Ar purging, this process is effectively irreversible. Addition of 2 equiv of [H(OEt)₂](BAr'₄) as a source of protons to the solution of **1b** did not alter the intensity of the absorption. Although stable for >6 h at −78 °C, **1b** rapidly decayed to a pale yellow solution upon warming to room temperature (Figure 1A).

Exposure of **2a** to O₂ under similar conditions resulted in an analogous irreversible color change from bright yellow to deep green (Figure 1B). The buildup of a broad ($\nu_{1/2} \approx 3400$ cm^{−1}) visible absorption of **2b** centered at ~670 nm ($\tilde{\nu} \approx 14\,900$ cm^{−1}; $\epsilon = 1700$ M^{−1} cm^{−1}) was monitored by UV–vis spectroscopy at −78 °C, affording $t_{1/2} \approx 7.7$ min under the conditions employed (gentle purging with O₂ for 1 min; see Supporting Information Figure S1). The thermal stability of **2b** is comparable to that of **1b**; no diminution in the intensity of the absorption band occurs up to 12 h at −78 °C. Upon warming to room temperature, however, **2b** decays to a bright yellow material (Figure 1B).

(b) Resonance Raman Spectroscopy. Raman spectra were obtained for **1b** and **2b** in CH₂Cl₂ at −78 °C. As shown in Figure 2, upon excitation at 647.1 nm, a strong resonance

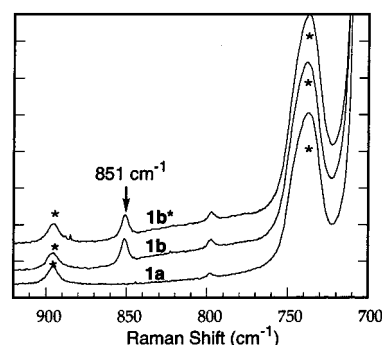


Figure 2. Resonance Raman spectra of fluid solutions of [Fe₂(μ-O₂CAr^{Tol})₂(O₂CAr^{Tol})₂(C₅H₅N)₂] (**1a**), **1a** + ¹⁶O₂ (**1b**), and **1a** + ¹⁸O₂ (**1b***) in CH₂Cl₂ at −78 °C. Excitation wavelength = 647.1 nm. Solvent features are labeled with asterisks.

enhanced peak appeared at 851 cm^{−1} for **1b**. This feature is absent both in the precursor compound **1a** and in the decomposition product of **1b**. Although this frequency falls into the right range for the O–O stretching mode of a (μ-peroxo)-diiron(III) species (see Supporting Information Table S1), no shift in the peak position was observed for samples prepared by reacting **1a** with either ¹⁸O-labeled dioxygen (**1b***) (Figure 2) or a 50:50 mixture of ¹⁶O:¹⁸O-labeled material under identical conditions (data not shown). A similar result was obtained for **2b**, which also exhibits a resonance enhanced vibration at 851 cm^{−1} (see Supporting Information Figure S2). Raman spectra were obtained for mixed-valence Fe^{II}Fe^{III} compounds **1mv** and **2mv**, which are one-electron chemical oxidation products of **1a** and **2a**, respectively (Scheme 2). Under conditions similar to those used for **1b** and **2b**, resonance enhanced peaks appear at 851 cm^{−1} for both **1mv** and **2mv** (see Supporting Information Figure S3).

(c) EPR Spectroscopy. Figure 3A displays the EPR spectra obtained for frozen CH₂Cl₂ samples of **2b**. A strong $g = 2$ signal and a less intense absorption at $g = 9.5$ were observed, which accounted for 70% of the total iron.³⁵ The signal at $g = 2$ arises from an $S = 1/2$ species (40% based on Fe₂), the g -anisotropy of which is similar to that of the antiferromagnetically (AF) coupled Fe^{III}Fe^{IV} core in RNR–R2, species X.^{11c,d,35} The signal at $g = 9.5$ originates from an $S = 9/2$ species (30% based on Fe₂), which was tentatively assigned as a mixed-valence Fe^{II}–Fe^{III} complex.³⁵ This assignment is now confirmed by the EPR spectrum of **2mv**, the independently synthesized, one-electron oxidized form of **2a**.

Figure 4 displays X-band (A) and Q-band (B) EPR spectra obtained for a frozen CH₂Cl₂ sample of **2mv**. The signal observed at $g = 9.5$ and 2.0 in X-band ($h\nu = 0.3$ cm^{−1}) perpendicular mode ($B_1 \perp B$) originates from a transition within the ground doublet of the $S = 9/2$ manifold. In the strong field limit, the transition occurs between $m_s = \pm 1/2$ states. The signal at $g = 4.3$ originates from trace contamination (~2%) of rhombic Fe(III) ($S = 5/2$). In Q-band perpendicular mode ($h\nu = 1.2$ cm^{−1}), three distinct transitions were observed. For $S = 9/2$ complexes with $E/D \sim 0$, we expect resonances to occur at $g = 10, 10,$ and 2 ($m_s = \pm 1/2$) and $g = 0, 0,$ and 6 ($m_s = \pm 3/2$), based on the standard diagrams of g_{obs} vs E/D .⁵¹ For $D \leq h\nu$, as is the case here, however, significant mixing of the doublets occurs, thus invalidating such diagrams. The signals at $g = 8.9$ and 2.9 originate from the ground- ($m_s = \pm 1/2$) and first-excited-state doublets ($m_s = \pm 3/2$) of the $S = 9/2$ manifold,

Scheme 2

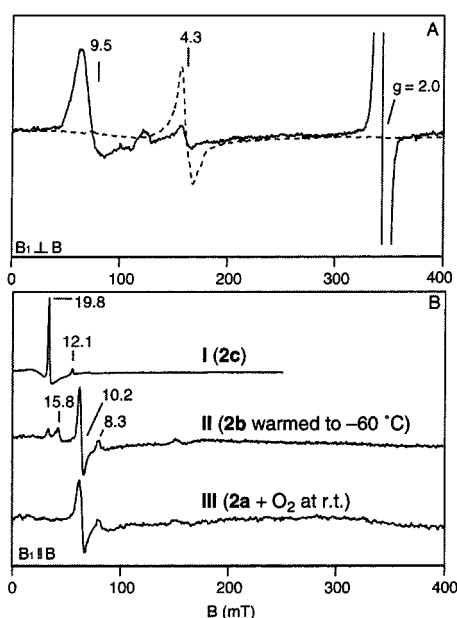
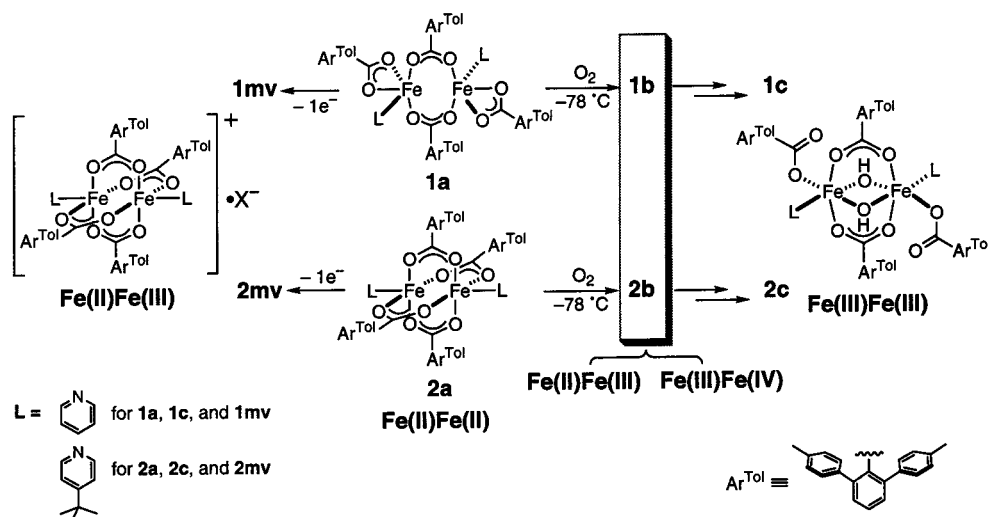


Figure 3. (A) Perpendicular mode ($B_1 \perp B$) X-band (9.62 GHz, 10 K) EPR spectra of a frozen CH_2Cl_2 solution sample of **2b** (solid line) and its thermolysis product (dashed line) prepared by thawing **2b** for 1 h under a He atmosphere at $-60^\circ C$ and re-freezing. (B) Parallel mode ($B_1 \parallel B$) X-band (9.26 GHz) EPR spectra of **2c** (I), thermolysis product of **2b** (II), and a sample prepared by exposing a CH_2Cl_2 solution of **2a** to dioxygen at room temperature and freezing (III). Spectra I and III were measured at 10 K; II was measured at 18 K.

respectively. The signal at $g = 4.2$ is novel and originates from an interdoubtlet transition between the $m_s = +1/2$ and $-3/2$ levels. The quantitative simulations overlaid on the data of Figure 4 confirm this assignment and give $D = 1.13\text{ cm}^{-1}$ and $E/D = 0.007$. The line widths are dominated by D -strain, which is modeled with distributions in the parameters D and E/D of Gaussian width σ_D and $\sigma_{E/D}$, respectively. The spectral fit determines both parameters independently, with values of $\sigma_D = 0.03\text{ cm}^{-1}$ and $\sigma_{E/D} = 0.004$. The EPR spectra of **2mv** and the $S = 9/2$ component in **2b** are essentially identical, indicating

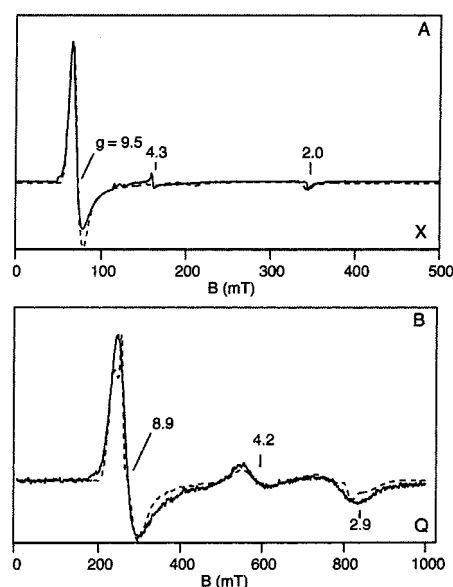


Figure 4. X-band (A) and Q-band (B) EPR spectra (solid lines) of a frozen CH_2Cl_2 solution sample of **2mv** measured at 11 and 6 K, respectively. Simulations (dashed lines) are calculated for $g = 2.0261$, $D = 1.13\text{ cm}^{-1}$, $\sigma_D = 0.03\text{ cm}^{-1}$, $E/D = 0.007$, and $\sigma_{E/D} = 0.004$. EPR conditions: frequency, 9.62 (X-band) and 34.2 GHz (Q-band); microwave power, 0.2 (X-band) and 0.02 mW (Q-band).

that a valence-delocalized $Fe^{II}Fe^{III}$ species is generated by the reaction between **2a** and dioxygen at $-78^\circ C$.

Anaerobic thawing at $-60^\circ C$ of the frozen CH_2Cl_2 solution sample of **2b** resulted in the total loss of the signals arising from $S = 1/2$ and $S = 9/2$ species and buildup of two new signals in the X-band EPR spectra (Figure 3). The signal at $g = 4.3$ (Figure 3A), constituting ca. 20% of the diiron starting material, originates from a rhombic $Fe(III)$ system ($S = 5/2$). Figure 3B displays the parallel mode EPR spectra of the $-60^\circ C$ thawed sample, showing the appearance of a signal at $g = 10.2$, which was tentatively assigned to an AF coupled $Fe^{III}Fe^{III}$ species. A similar $g = 10.2$ signal was observed when the reaction between **2a** and dioxygen was conducted at room temperature. This signal, however, is different from the $g = 19.8$ signal of **2c**, which arises from a transition within the $S = 5$ manifold of a ferromagnetically coupled $Fe^{III}Fe^{III}$ center. This result confirms that the crystallographically characterized com-

- (51) Krebs, C.; Davydov, R.; Baldwin, J.; Hoffman, B. M.; Bollinger, J. M., Jr.; Huynh, B. H. *J. Am. Chem. Soc.* **2000**, *122*, 5327–5336.
 (52) Valentine, A. M.; Tavares, P.; Pereira, A. S.; Davydov, R.; Krebs, C.; Hoffman, B. M.; Edmondson, D. E.; Huynh, B. H.; Lippard, S. J. *J. Am. Chem. Soc.* **1998**, *120*, 2190–2191.

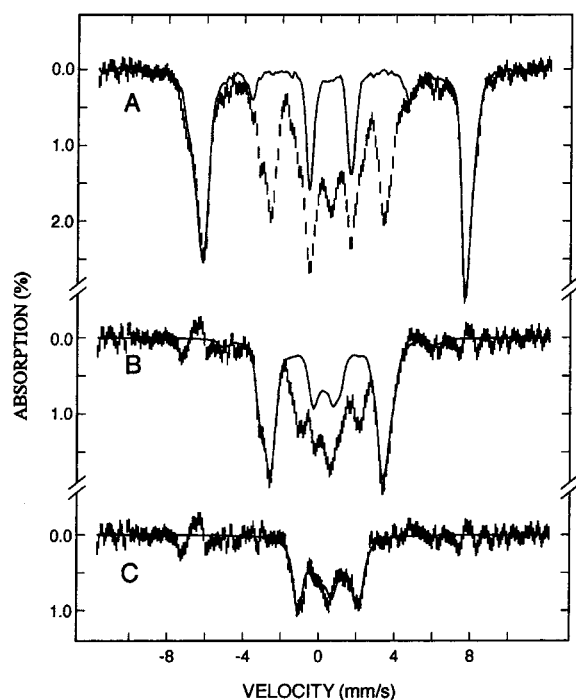


Figure 5. Deconvolution of the Mössbauer spectrum of the solid powder sample of **2b** recorded at 4.2 K in an applied field of 8 T. (A) Raw data of **2b** (hatch marks) and the spectrum of a solid sample of $[\text{Fe}_2(\mu\text{-O}_2\text{CAR}^{\text{Tol}})_4(4\text{-BuC}_5\text{H}_4\text{N})_2](\text{PF}_6)$ (**2mv**) (solid line) scaled to 45% of the absorption intensity of the hatch-marked spectrum. (B) The hatch-marked spectrum is generated by subtracting the solid-line spectrum of A from the hatch-marked spectrum of A. The solid line is a theoretical simulation of the $\text{Fe}^{\text{III}}\text{Fe}^{\text{IV}}$ species using parameters from Table 1 and corresponds to 36% of the total iron absorption. (C) The hatch-marked spectrum is generated by subtracting the solid-line spectrum of B from the hatch-marked spectrum of B. The solid line is a theoretical simulation using $\delta = 0.54$ mm/s, $\Delta E_Q = 1.05$ mm/s, $\eta = 0.4$, and line-width $\Gamma = 0.55$ mm/s, and assuming diamagnetism.

plex **2c** (vide infra) is not an immediate oxygenation product of **2a**.

(d) Mössbauer Spectroscopy. Previous Mössbauer studies of **2b** identified three major diiron species.³⁵ Among these components, only the species having $S = 1/2$ spin state has a strong dependence on the orientation of the applied field with respect to the direction of the γ -rays. The presence of the AF coupled $\text{Fe}^{\text{III}}\text{Fe}^{\text{IV}}$ species (36% based on Fe_2) was thus revealed from Mössbauer spectra recorded at 4.2 K with a 50 mT magnetic field applied parallel and perpendicular to the γ -rays.³⁵ In a complementary approach, the Mössbauer spectra of **2b** were now recorded in higher magnetic fields (4–8 T) and deconvoluted into three spectral components through an iterative process.

(1) Spectral Deconvolution. Shown in Figure 5A is the Mössbauer spectrum of a solid sample of **2b** (hatched lines) recorded at 4.2 K in a magnetic field of 8 T applied parallel to the γ -ray beam. The two well-resolved outermost lines at -6.2 and $+7.7$ mm/s are closely matched, in both positions and shapes, by those of the spectrum of a solid sample of **2mv** (solid line) recorded under identical experimental conditions,⁴⁰ indicating that they arise from the valence-delocalized $S = 9/2$ $\text{Fe}^{\text{II}}\text{Fe}^{\text{III}}$ species. By matching the intensities of these outer lines to that of the spectrum of solid **2b**, it is estimated that 45% of the total iron in the green mixture is in the form of $[\text{Fe}_2(\mu\text{-O}_2\text{CAR}^{\text{Tol}})_4(4\text{-BuC}_5\text{H}_4\text{N})_2]^+$ (see the caption of Figure 5A), an amount slightly higher than that ($\sim 34\%$) estimated from the 50 mT spectral analysis.³⁵

Removal of the contribution of $[\text{Fe}_2(\mu\text{-O}_2\text{CAR}^{\text{Tol}})_4(4\text{-BuC}_5\text{H}_4\text{N})_2]^+$ from the raw data of **2b** yields the spectrum shown in Figure 5B. The lines at -2.7 and $+3.4$ mm/s are well-resolved and can be assigned to the valence-trapped $\text{Fe}^{\text{III}}\text{Fe}^{\text{IV}}$ species. The solid line shown in Figure 5B is a theoretical simulation of this species using the parameters presented in Table 1 and accounts for 36% of the total iron absorption. Removal of this component from the spectrum shown in Figure 5B yields the spectrum (Figure 5C) arising from an $\text{Fe}^{\text{III}}\text{Fe}^{\text{III}}$ species, which shows features at -1 , $+0.5$, and $+2.1$ mm/s. The theoretical simulation of this component, which is plotted as a solid line in Figure 5C, was calculated by using the parameters given in the caption of Figure 5 and assuming diamagnetism ($S = 0$). The Mössbauer parameters, which are typical of N/O-coordinate high-spin $\text{Fe}(\text{III})$ ions,^{53–55} and the diamagnetism are consistent with the assignment that this component represents an AF coupled $\text{Fe}^{\text{III}}\text{Fe}^{\text{III}}$ species. This component accounts for approximately 19% of the total intensity, and the large line width indicates the presence of some microheterogeneity.

(2) Valence-Delocalized $\text{Fe}^{\text{II}}\text{Fe}^{\text{III}}$ Species. As mentioned above, a major spectral component observed in the spectrum of **2b** recorded at 4.2 K and 8 T is accurately represented by the spectrum of a solid sample of **2mv** recorded under the same conditions. This result indicates that **2b** includes the valence-delocalized $\text{Fe}^{\text{II}}\text{Fe}^{\text{III}}$ cation $[\text{Fe}_2(\mu\text{-O}_2\text{CAR}^{\text{Tol}})_4(4\text{-BuC}_5\text{H}_4\text{N})_2]^+$. To illustrate this point, a spectrum of solid **2mv** (Figure 6A) is compared to the $\text{Fe}^{\text{II}}\text{Fe}^{\text{III}}$ component in **2b** (Figure 6B). The similarities between these two spectra are obvious. In Figure 6C is shown the $\text{Fe}^{\text{II}}\text{Fe}^{\text{III}}$ component in **2b** recorded at 4.2 K in an applied field of 4 T. This spectrum consists of a single six-line pattern, indicating that both iron sites contribute identical Mössbauer spectra. This observation demonstrates unequivocally that the $\text{Fe}^{\text{II}}\text{Fe}^{\text{III}}$ component in **2b** is a valence-delocalized cluster, $[\text{Fe}_2(\mu\text{-O}_2\text{CAR}^{\text{Tol}})_4(4\text{-BuC}_5\text{H}_4\text{N})_2]^+$. EPR and SQUID measurements demonstrate that $[\text{Fe}_2(\mu\text{-O}_2\text{CAR}^{\text{Tol}})_4(4\text{-BuC}_5\text{H}_4\text{N})_2]^+$ has a $S = 9/2$ ground state.⁴⁰ Furthermore, the zero-field parameters have been determined by EPR spectroscopy and are $D = 1.2$ cm⁻¹ and $E/D = 0.013$.³⁵ For the analysis of the Mössbauer spectrum of the $[\text{Fe}_2(\mu\text{-O}_2\text{CAR}^{\text{Tol}})_4(4\text{-BuC}_5\text{H}_4\text{N})_2]^+$ component in **2b**, we use eqs 3 and 4 and assume that the electronic relaxation is slow compared to the ⁵⁷Fe nuclear Larmor precession and that $E/D = 0.013$. With these assumptions, the parameter D can be determined from the field-dependent Mössbauer data for the following reasons. The size of the magnetic splitting of a Mössbauer spectrum depends on the magnitude of the internal field, $\langle \mathbf{S} \rangle \cdot \mathbf{A}$, where $\langle \mathbf{S} \rangle$ represents the spin expectation value at the Fe sites. For the case of $D \approx g\beta H$, which describes the current situation, the expectation values for the three components, $\langle S_x \rangle$, $\langle S_y \rangle$, and $\langle S_z \rangle$, of $\langle \mathbf{S} \rangle$ depend sensitively on the ratio of $D/g\beta H$. Consequently, it is possible to determine the value of D from the field dependence of the spectra. Such an analysis gives $D = 1.2 \pm 0.2$ cm⁻¹, which is in excellent agreement with the value determined by EPR spectroscopy (vide supra).

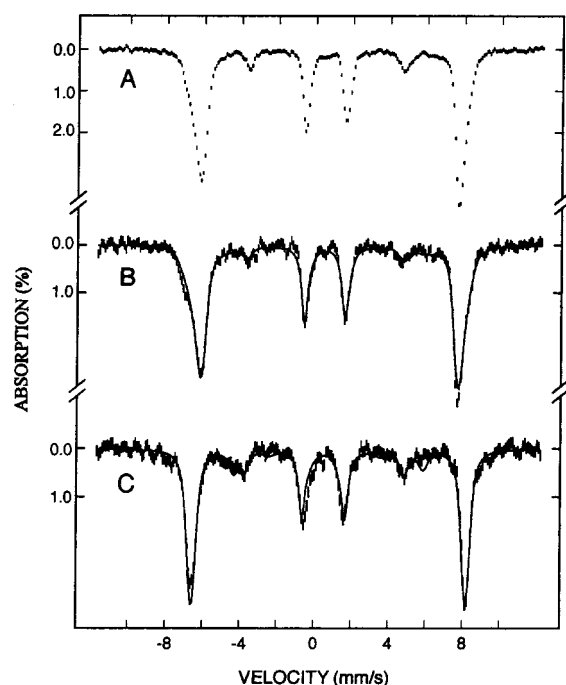
(53) Kurtz, D. M., Jr. *Chem. Rev.* **1990**, *90*, 585–606.

(54) Gütllich, P.; Ensling, J. *Inorganic Electronic Structure and Spectroscopy*; Solomon, E. I., Lever, A. B. P., Eds.; John Wiley & Sons: New York, 1999; Vol. 1, pp 161–211.

(55) Münck, E. *Physical Methods in Bioinorganic Chemistry: Spectroscopy and Magnetism*; Que, L., Jr., Ed.; University Science Books: Sausalito, CA, 2000; pp 287–319.

Table 1. Mössbauer Parameters of the Fe^{III}Fe^{IV} Component in **2b** and Related Valence-Trapped Fe^{III}Fe^{IV} Centers Having a *S* = 1/2 Ground State

		δ (mm/s)	ΔE_Q (mm/s)	η	A_{xx} (MHz)	A_{yy} (MHz)	A_{zz} (MHz)	ref
2b	Fe(III)	0.56	0.9	−0.3	−75	−70.5	−75	this work
	Fe(IV)	0.19	0.8	−1	26	37.5	23.8	
RNR−R2, species X	Fe(III)	0.56	−0.9	0.5	−74.2	−72.2	−73.2	11a,c
	Fe(IV)	0.26	−0.6	2.7	27.5	36.8	36.8	
MMOH−Q _x	Fe(III)	0.48	−0.9	0.2	−70	−75	−75	52
	Fe(IV)	0.14	−0.6	0.9	26	30	32	
[Fe ₂ (μ-O) ₂ (6-Me-TPA) ₂] ³⁺ ³⁷	Fe(III)	0.48	1.6	1.0	−64.5	−64.5	−64.5	32b
	Fe(IV)	0.08	0.5	1.0	20	36.5	36.5	

**Figure 6.** Mössbauer spectra (4.2 K) of [Fe₂(μ-O₂CAR^{Tol})₄(4-^tBuC₅H₄N)₂](PF₆) (**2mv**) in the form of solid (A) and the Fe^{II}Fe^{III} component in **2b** (B and C). The spectra in A and B are recorded in a parallel applied field of 8 T, and the spectrum in C is recorded in 4 T. The spectra in B and C were prepared by removing the contributions of the Fe^{III}Fe^{IV} (36%) and the Fe^{II}Fe^{III} species (19%) from the raw data using theoretical spectra of Fe^{III}Fe^{IV} and the Fe^{II}Fe^{III} species simulated with parameters listed in Table 1 and quoted in the caption of Figure 5.

From the analysis of the Mössbauer spectra, other characteristic parameters can also be determined (Table 2). Theoretical simulations using these parameters are plotted in Figure 6 as solid lines overlaid with the corresponding experimental spectra. The agreement between theory and experiment is excellent. In Table 2, the parameters determined for [Fe₂(μ-O₂CAR^{Tol})₄(4-^tBuC₅H₄N)₂]⁺ are compared with those of related valence-delocalized Fe^{II}Fe^{III} compounds. The Mössbauer parameters of a valence-delocalized compound are the arithmetic means of those of the corresponding pure Fe(II) and Fe(III) sites in the same ligand environment.⁵⁶ Accordingly, the ranges of isomer shifts (0.74–0.84 mm/s) and magnitudes of quadrupole splittings (1.86–2.14 mm/s) observed for valence-delocalized *S* = 9/2 Fe^{II}Fe^{III} compounds are between the typical values for N/O coordinated high-spin Fe(III) and N/O coordinated high-spin Fe(II) sites.^{57–60} In comparison with these values, the isomer shift, δ = 0.65 mm/s, and quadrupole splitting, $|\Delta E_Q|$ = 0.63 mm/s, determined for **2mv**, are significantly smaller. The smaller isomer shift observed for **2mv** can in part be explained by the fact that the iron centers are five coordinate. The origin of the

smaller quadrupole splitting, however, is unclear. For the compound [Fe₂(μ-OH)₃(Me₃TACN)₂]²⁺³⁷ the value of the quadrupole splitting, ΔE_Q = −2.14 mm/s, was attributed to the delocalized electron being in a *d_{z²}* orbital.⁵⁷ More recently, the interaction between the two Fe-centered *d_{z²}* orbitals (with the Fe–Fe vector defining the *z*-axis) was identified as a mechanism for promoting the electron delocalization between the two Fe sites.⁶¹ The reduced magnitude of the quadrupole splitting in **2mv**, ΔE_Q = −0.63 mm/s, however, indicates that the orbital ground state of **2mv** is not a pure *d_{z²}* orbital, but rather a quantum admixture, possibly of *d_{z²}* and *d_{xy}* orbitals. Since *d_{z²}* and *d_{xy}* orbitals generate opposite electric field gradients,⁶² a quantum admixture of these two orbitals would reduce the magnitude of the quadrupole splitting. DFT calculations are currently in progress to gain further insights into the electronic structure of **2mv** and to understand these unusual Mössbauer parameters.⁶³

(3) Valence-Trapped Fe^{III}Fe^{IV} Species. Figure 7 displays the Mössbauer spectra (hatch marks) of the Fe^{III}Fe^{IV} species in **2b** recorded at 4.2 K in a parallel applied field of 4 (A) or 8 T (B). These spectra can be deconvoluted into two equal intensity spectral components corresponding to two valence-localized Fe sites. Each site contributes approximately 18% of the total iron absorption. Characteristic parameters obtained for the two Fe sites are listed in Table 1, and theoretical simulations of each individual component are displayed in Figure 7 above the experimental spectra. The solid lines overlaid with the experimental spectra are the superpositions of the two individual spectral components. The observation that the magnetic splitting of one of the components (depicted as dashed lines above the data) *increases* whereas that of the other component (shown as solid lines above the data) *decreases* with increasing applied field demonstrates the antiparallel orientation of the individual spins of the Fe sites in the ground state and establishes unambiguously the AF coupling nature of Fe^{III}Fe^{IV}. The different field dependence is reflected in different signs of the *A*-tensors. The Fe site with a negative *A*-tensor has an isomer shift, δ = 0.56 mm/s, typical of a high-spin Fe(III) ion with N/O coordination.^{53–55} In accord with this assignment, the *A*-tensor of this site is rather isotropic, as expected for high-spin Fe(III) compounds. The second Fe site has a positive *A*-tensor with

(56) Blondin, B.; Girerd, J.-J. *Chem. Rev.* **1990**, *90*, 1359–1376.(57) Ding, X.-Q.; Bominaar, E. L.; Bill, E.; Winkler, H.; Trautwein, A. X.; Drücke, S.; Chaudhuri, P.; Wieghardt, K. *J. Chem. Phys.* **1990**, *92*, 178–186.(58) Dutta, S. K.; Ensling, J.; Werner, R.; Flörke, U.; Haase, W.; Gütlisch, P.; Nag, K. *Angew. Chem., Int. Ed. Engl.* **1997**, *36*, 152–155.(59) Hagadorn, J. R.; Que, L., Jr.; Tolman, W. B.; Prisecaru, I.; Münck, E. *J. Am. Chem. Soc.* **1999**, *121*, 9760–9761.

(60) Krebs, C. Ph.D. Thesis, Ruhr-Universität Bochum, Germany, 1997.

(61) Gamelin, D. R.; Bominaar, E. L.; Kirk, M. L.; Wieghardt, K.; Solomon, E. I. *J. Am. Chem. Soc.* **1996**, *118*, 8085–8097.(62) Rodriguez, J. H.; Ok, H. N.; Xia, Y.-M.; Debrunner, P. G.; Hinrichs, B. E.; Meyer, T.; Packard, N. H. *J. Phys. Chem.* **1996**, *100*, 6849–6862.

(63) Rodriguez, J. H.; Lee, D.; Lippard, S. J. Unpublished results.

Table 2. Mössbauer Parameters of the Fe^{II}Fe^{III} Component in **2b**, [Fe₂(μ-O₂CAr^{Tol})₄(4-^tBuC₅H₄N)₂]⁺, and Related Valence-Delocalized Fe^{II}Fe^{III} Centers Having a *S* = 9/2 Ground State

	δ (mm/s)	Δ <i>E</i> ₀ (mm/s)	η	<i>A</i> _{xx} (MHz)	<i>A</i> _{yy} (MHz)	<i>A</i> _{zz} (MHz)	ref
[Fe ₂ (μ-O ₂ CAr ^{Tol}) ₄ (4- ^t BuC ₅ H ₄ N) ₂] ⁺	0.65	−0.63	0	−15.2	−15.8	−20.7	this work
[Fe ₂ (μ-OH) ₃ (Me ₃ TACN) ₂] ²⁺ 37	0.74	−2.14	0	−14.5	−14.5	−18.5	57
[PhB{Fe ₂ (μ-dfmp) ₃ }BPh] ³⁷	0.82	−1.86	0	−14.8	−14.8	−17.0	60
[L ¹ Fe ₂ (μ-OAc) ₂] ⁺ 37	0.84	2.09	0.1	a	a	a	58
[Fe ₂ (μ-O ⁱ Pr) ₂ (μ-O ₂ CAr ^{Mes})(O ₂ CAr ^{Mes}) ₂] ³⁷	0.76	2.0	0.7	a	a	a	59

^a Only the internal fields, 43.5 T for ref 58 and 41.0 T for ref 59, along the magnetic uniaxial have been reported.

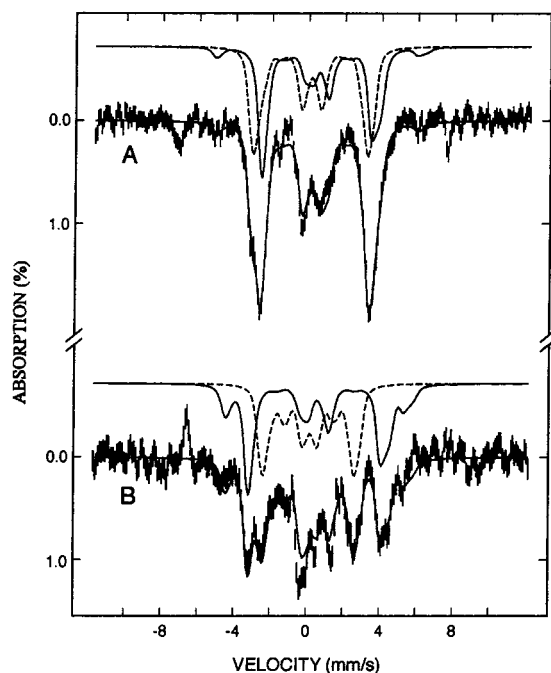


Figure 7. Mössbauer spectra (4.2 K) of the Fe^{II}Fe^{IV} component in the solid powder sample of **2b** in applied fields of 4 (A) and 8 T (B). The hatch-marked spectra were prepared by removing the contributions of Fe^{II}Fe^{III} (45%) and the Fe^{II}Fe^{III} cluster (19%) from the raw data using theoretical spectra simulated with parameters listed in Table 2 and quoted in the caption of Figure 5. The solid lines overlaid with the experimental data are theoretical simulations of Fe^{II}Fe^{IV} using parameters listed in Table 1. The spectra of the Fe(III) and Fe(IV) sites are plotted above the experimental data as solid and dashed lines, respectively.

significant anisotropy (about 30%). The isomer shift of this site, δ = 0.19 mm/s, is below the typical range for high-spin Fe(III) ions and is assigned to a high-spin Fe(IV) site. The anisotropy of the *A*-tensor is consistent with this assignment. Similar valence-trapped Fe^{II}Fe^{IV} clusters have been observed for the RNR–R2 reaction intermediate X,^{11a,c} the state MMOH–Q_X, which is a cryoreductively generated one-electron-reduced intermediate Q from the MMOH reaction cycle,⁵² and the model compound [Fe₂(μ-O)₂(6-Me-TPA)₂]³⁺.^{32b,37} As presented in Table 1, the Mössbauer parameters of the Fe^{II}Fe^{IV} component in **2b** compare very well with those of RNR–R2, species X and MMOH–Q_X. This result indicates that, compared with the nitrogen-rich donor atom sets in [Fe₂(μ-O)₂(6-Me-TPA)₂]³⁺,^{32b,37} the coordination environment of the enzyme intermediate is better reproduced by the tetracarboxylate ligand system employed in this investigation.

(e) Manometric Studies. Dioxygen uptake was monitored by manometric measurements (three replicate runs) for the reaction between O₂ and **2a** in CH₂Cl₂ at −78 °C. Compound **2a** consumed 0.75 ± 0.1 equiv of O₂ to provide **2b**. This substoichiometric consumption of dioxygen contrasts with the

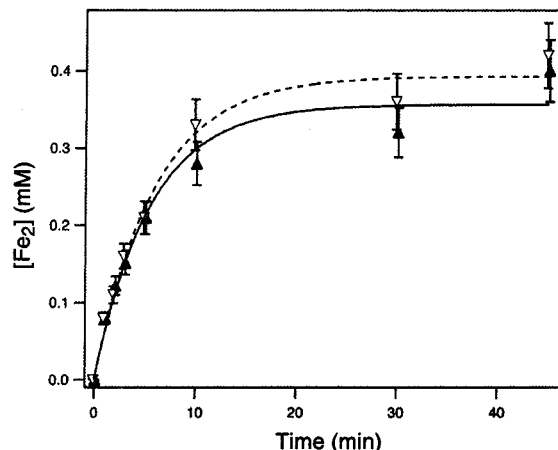


Figure 8. Time-dependent development of the *S* = 1/2 (▽) and *S* = 9/2 (▲) components in **2b** as determined by X-band EPR spectra of freeze-quenched samples prepared by oxygenating **2a** (1.12 mM) in CH₂Cl₂ at −78 °C. Fits to experimental data for the *S* = 1/2 (dashed line) and *S* = 9/2 (solid line) species indicate *k*_{obs} = 0.18 ± 0.02 min^{−1}. Spin quantitation was carried out as described in the Experimental Section.

1:1 stoichiometry observed for the formation of discrete (peroxo)diiron(III) species in other studies.^{17b,20}

(f) EPR Kinetic Studies. The relatively slow formation rate of paramagnetic intermediates at −78 °C allowed us to monitor the buildup of *S* = 1/2 and *S* = 9/2 components in **2b** by X-band EPR spectroscopy as a function of time. Identical solution samples of **2a** were prepared in CH₂Cl₂, and reactions were initiated by injecting known amounts of dioxygen at −78 °C. Following different incubation times at −78 °C, each sample was frozen at 77 K and analyzed by X-band EPR spectroscopy. Shown in Figure 8 is a plot of the concentration of *S* = 1/2 and *S* = 9/2 components as a function of time. The concentrations were determined from quantitation of the EPR signals at *g* = 2 and 9.5, respectively. Both components build up at the same rate and exist in the same relative amounts throughout the reaction. A pseudo-first-order fit to the data is shown in Figure 8, which gave *k*_{obs} = 0.18 ± 0.02 min^{−1} at −78 °C. This result is strong evidence that the processes leading to the formation of *S* = 1/2 and *S* = 9/2 components in **2b** are coupled to one another. The reaction approaches completion at >45 min, affording ca. 38% of the *S* = 1/2 and 36% of *S* = 9/2 components (based on **2a**).

The presence of a proton source significantly affects the development of the *S* = 1/2 and *S* = 9/2 species. Figure S4 of the Supporting Information shows the EPR spectra of **2b** quenched 5 min after oxygenation at −78 °C. When 0.5 equiv of [H(OEt)₂]₂(BAR'₄) was added to **2a** prior to reaction with O₂, the amount of the *S* = 9/2 component formed is comparable to that in the absence of a proton source. The amount of the *S* = 1/2 component, however, is drastically reduced from 19%

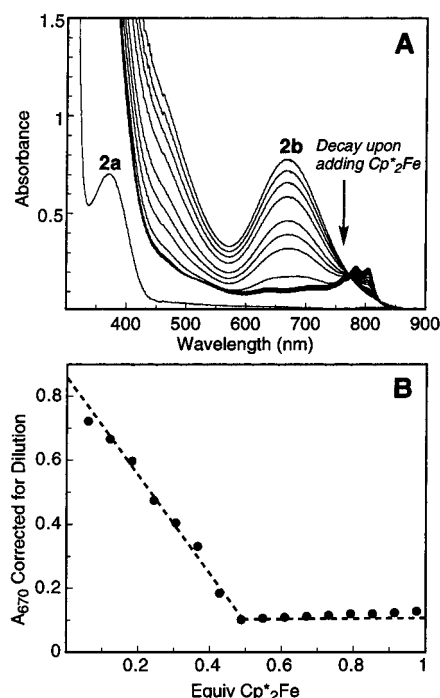


Figure 9. (A) Representative UV–vis spectra for the reaction of **2b** with Cp^*Fe in CH_2Cl_2 at -78°C . The spectral traces track the decay of the $\lambda_{\text{max}} = 670$ chromophore upon addition of Cp^*Fe . (B) A plot of A_{670} versus the equivalents (per **2a**) of Cp^*Fe added. The values are corrected for dilution.

(without H^+) to 2% (with H^+) of the diiron(II) starting material **2a**. This result indicates that the $\text{Fe}^{\text{III}}\text{Fe}^{\text{IV}}$ species has ligand fragments that are susceptible to protonation. Changes in the metal oxidation states may be triggered by ligand protonation, resulting in the loss of the AF coupled $\text{Fe}^{\text{III}}\text{Fe}^{\text{IV}}$ component in **2b**.

Reactions of the Oxygenation Intermediates with External Reagents. (a) Cp_2Fe and Cp^*Fe . Addition of Cp_2Fe to a CH_2Cl_2 solution of **2b** at -78°C did not perturb the electronic absorption at 670 nm, whereas Cp^*Fe completely abolished this transition. This finding requires that the reduction potential of **2b** lie between -130 mV and $+460$ mV vs SCE.⁶⁴ A redox titration of **2b** was therefore carried out by monitoring the decay of the 670 nm absorption band as a function of Cp^*Fe added under Ar at -78°C . Typical UV–vis traces are displayed in Figure 9. An average oxidizing equivalent of 0.45 ± 0.04 (three replicate runs) was determined for the $\lambda_{\text{max}} = 670$ nm chromophore in **2b**.

(b) Oxidation of Phenol Substrates. Both **1b** and **2b** act as one-electron oxidants and proton acceptors. Addition of 2.2 equiv of 2,4,6-tri-*tert*-butylphenol to a CH_2Cl_2 solution of **1b** at -78°C did not result in any change in the UV–vis spectra. Upon warming to room temperature, however, absorption peaks develop at 383 and 401 nm, which are characteristic of the 2,4,6-tri-*tert*-butylphenoxyl radical.^{34,65} Formation of the phenoxyl radical was further confirmed by an EPR signal at $g = 2.005$ in a sample prepared under similar conditions.³⁴ At room temperature, the reaction mixture remains blue. When 2,4-di-*tert*-butylphenol was allowed to react with **2b**, the 3,3',5,5'-tetra-*tert*-butyl-1,1'-bi-2,2'-phenol coupling product was obtained

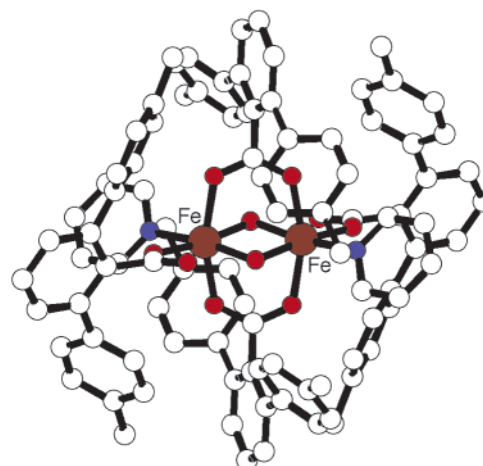


Figure 10. Ball and stick representation of the solid-state structure of $[\text{Fe}_2(\mu\text{-OH})_2(\mu\text{-O}_2\text{CAR}^{\text{Tol}})_2(\text{O}_2\text{CAR}^{\text{Tol}})_2(\text{C}_5\text{H}_5\text{N})_2]$ (**1c**) generated using the crystallographic coordinates.³⁴

in $\sim 40\%$ yield based on **2a**. Upon warming from -78°C to room temperature, the color of the solution turned blue, as for **1b**. A mononuclear iron(III) complex $[\text{Fe}(\text{O}_2\text{CAR}^{\text{Tol}})_2(2,4\text{-}^t\text{Bu}_2\text{C}_6\text{H}_3\text{O})(4\text{-}^t\text{BuC}_5\text{H}_4\text{N})]$ (Figure S5 of the Supporting Information)⁶⁶ was isolated by vapor diffusion of pentanes into the reaction mixture, indicating that the blue color arises from a phenoxide-to-iron(III) LMCT band.⁶⁷ No 2,4-di-*tert*-butylphenol coupling product was detected when a similar reaction was carried out with the $\text{Fe}^{\text{II}}\text{Fe}^{\text{III}}$ compound **2mv**.

Di(μ -hydroxo)di(μ -carboxylato)diiron(III) Complexes $[\text{Fe}_2(\mu\text{-OH})_2(\mu\text{-O}_2\text{CAR}^{\text{Tol}})_2(\text{O}_2\text{CAR}^{\text{Tol}})_2\text{L}_2]$, $\text{L} = \text{C}_5\text{H}_5\text{N}$ (1c**) and 4-*tert*-butyl-5-phenylpyridine (**2c**).** **(a) Synthesis and Structural Characterization.** Quadruply bridged diiron(III) complexes **1c** and **2c** were isolated in good to excellent yields (75–90%) following vapor diffusion of pentanes into the thermal decomposition product(s) of **1b** and **2b** in CH_2Cl_2 , respectively.^{34,35} The solid-state structure of **1c** is shown in Figure 10; selected bond lengths and angles in **1c** and **2c** are listed in Table 3. In both cases, two chemically identical but crystallographically inequivalent molecules were identified in the unit cell, each sitting on an inversion center. The structures of **1c** and **2c** are essentially the same, having two iron atoms bridged by two hydroxide and two μ -1,3-carboxylate ligands. Assignment of the single atom bridging ligands as hydroxide is supported by the Fe–O distances of 1.949(3)–2.012(2) Å, as well as by the location and refinement of the associated hydrogen atoms in the X-ray structure determination. The $\text{Fe}\cdots\text{Fe}$ distances of 2.8322(8)–2.8843(9) Å in **1c** and **2c** are significantly below the range (3.089(2)–3.155(3) Å) obtained for doubly bridged $\{\text{Fe}_2(\mu\text{-OH})_2\}^{4+}$ cores,^{68,69} and lie between 2.95(1) and 2.714(2) Å observed for $\{\text{Fe}_2(\mu\text{-O})(\mu\text{-OH})\}^{3+70}$ and $\{\text{Fe}_2(\mu\text{-O})_2\}^{2+71}$ core fragments, respectively. This trend nicely demonstrates the

(64) Connelly, N. G.; Geiger, W. E. *Chem. Rev.* **1996**, *96*, 877–910.

(65) Altwicker, E. R. *Chem. Rev.* **1967**, *67*, 475–531.

(66) Crystal data for $[\text{Fe}(\text{O}_2\text{CAR}^{\text{Tol}})_2(2,4\text{-}^t\text{Bu}_2\text{C}_6\text{H}_3\text{O})(4\text{-}^t\text{BuC}_5\text{H}_4\text{N})]$: space group $P2_1/n$ with $a = 17.9762(6)$ Å, $b = 14.4378(5)$ Å, $c = 23.7130(7)$ Å, $\beta = 104.1780(10)^\circ$, $V = 5966.9(3)$ Å³, $Z = 4$, $R = 7.76\%$, $R_w = 17.28\%$.

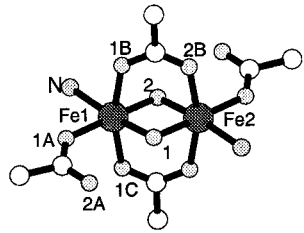
(67) Lever, A. B. P. *Inorganic Electronic Spectroscopy*, 2nd ed.; Elsevier Science Publishers B. V.: Amsterdam, The Netherlands, 1984.

(68) Borer, L.; Thalken, L.; Ceccarelli, C.; Glick, M.; Zhang, J. H.; Reiff, W. M. *Inorg. Chem.* **1983**, *22*, 1719–1724.

(69) Thich, J. A.; Ou, C. C.; Powers, D.; Vasiliou, B.; Mastropaolo, D.; Potenza, J. A.; Schugar, H. J. *J. Am. Chem. Soc.* **1976**, *98*, 1425–1433.

(70) Zang, Y.; Pan, G.; Que, L., Jr.; Fox, B. G.; Münck, E. *J. Am. Chem. Soc.* **1994**, *116*, 3653–3654.

(71) Zang, Y.; Dong, Y.; Que, L., Jr.; Kauffmann, K.; Münck, E. *J. Am. Chem. Soc.* **1995**, *117*, 1169–1170.

Table 3. Selected Bond Lengths (Å) and Angles (deg) for **1c** and **2c**^a


	1c		2c	
	molecule 1	molecule 2	molecule 1	molecule 2
Fe1...Fe2	2.8843(9)	2.8473(8)	2.8432(8)	2.8322(8)
Fe1—O1	1.986(2)	1.976(2)	1.949(3)	1.955(2)
Fe1—O2	2.012(2)	1.969(3)	1.957(3)	1.955(2)
Fe1—O1A	1.970(2)	1.964(2)	1.966(2)	1.965(2)
Fe1—O1B	2.076(2)	2.096(2)	2.082(2)	2.081(2)
Fe1—O1C	2.040(2)	2.060(2)	2.055(2)	2.048(2)
Fe1—N	2.148(3)	2.144(3)	2.136(3)	2.127(3)
O1...O2A	2.888(3)	2.773(4)	2.725(4)	2.736(4)
Fe1—O1—Fe2	92.34(10)	92.38(11)	93.42(12)	92.82(11)
O1—Fe1—O2	87.66(10)	87.62(11)	86.58(12)	87.18(11)

^a Numbers in parentheses are estimated standard deviations of the last significant figures.

systematic shortening of the metal...metal distances in the {M₂L₂}ⁿ⁺ rhombic cores by decreasing the M—L distances, as well as by increasing the number of bridging units. For comparison, an Fe...Fe distance of 2.9788(6) Å was obtained for the triply bridged {Fe₂(μ-OH)₂(μ-O₂CR)}³⁺ unit in [Fe₂(μ-OH)₂(μ-O₂CAr^{Tol})(O₂CAr^{Tol})₃(N-Bnen)(N,N-Bn₂en)],⁷² the first structural model compound of the diiron(III) core in MMOH. The Fe—O_{hydroxide}—Fe angles in **1c** and **2c** range from 92.34(10) to 93.42(12)°. The two terminal η¹-carboxylate ligands are hydrogen bonded to the bridging hydroxide groups (O_{hydroxide}...O_{carboxylate} = 2.725(4)–2.888(3) Å). Binding of the two pyridine ligands, disposed anti across the Fe—Fe vector, completes the pseudo-octahedral coordination spheres of the two iron(III) centers.

For edge-shared octahedral metal centers, quadruply bridged units consisting of two hydroxide and two Ar^{Tol}CO₂[−] ligands can only be accommodated by a trans-disposition of the μ-1,3 carboxylates across the {M₂(μ-OH)₂}ⁿ⁺ plane, a configuration that alleviates steric interactions between the *p*-tolyl groups. An analogous dicobalt(III) complex was recently synthesized and structurally characterized,⁷³ suggesting that the {M₂(μ-OH)₂(μ-O₂CR)₂}²⁺ core fragment may be a general structural motif for quadruply bridged trivalent dimetallics supported by Ar^{Tol}CO₂[−] and related ligands.

(b) Mössbauer, EPR, and Magnetic Properties. Zero-field Mössbauer spectra of both solid and solution samples of **2c** were collected at 4.2 K. The spectrum of powdered **2c** displays a relatively sharp (Γ = 0.36–0.39 mm s^{−1}) quadrupole doublet (Figure 11A) with δ = 0.49(2) mm s^{−1} and ΔE_Q = 1.01(2) mm s^{−1}, values typical for high-spin Fe(III) ions.^{53–55} Identical Mössbauer parameters were obtained for the frozen THF solution states (Figure 11B). Although the peaks are significantly broadened (Γ = 0.52–0.53 mm s^{−1}) in the latter case, this result indicates that the integrity of the diiron(III) core is maintained in solution.

Compounds **1c** and **2c** display weak ferromagnetic coupling, affording S = 5 ground spin states. An EPR signal from a

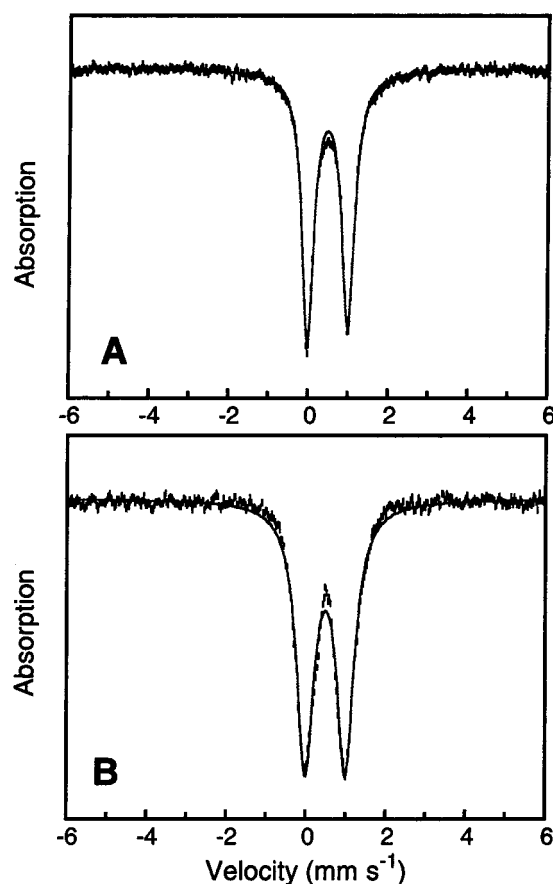


Figure 11. Zero-field Mössbauer spectra (experimental data (•), calculated fit (—)) recorded at 4.2 K for [Fe₂(μ-OH)₂(μ-O₂CAr^{Tol})₂(O₂CAr^{Tol})₂(4-BuC₅H₄N)₂] (**2c**) (A) as a solid-state sample and (B) as a THF frozen solution sample.

transition within an S = 5 manifold was observed for **2c**. This signal is shown in Figure 3B (spectrum I), and its temperature dependence indicates that it originates from the ground doublet or a nearby state. Plots of the effective magnetic moment (μ_{eff}) and molar susceptibility (χ_M) versus temperature for **1c** and **2c** are presented in Figures 12 and S6 (Supporting Information), respectively. At temperatures above ~150 K, the effective magnetic moment is essentially constant at 8.4 μ_B (for **1c**) and 8.5 μ_B (for **2c**), values consistent with the presence of two uncoupled S = 5/2 centers with g = 2.00 (calculated spin-only value of μ_{eff} = 8.37 μ_B). Upon lowering the temperature, μ_{eff} gradually increases to 10.23 μ_B and 10.37 μ_B at 5 K for **1c** and **2c**, respectively. These values are close to the theoretical moment of 10.95 μ_B calculated for an S_{tot} = 5 spin state arising from two ferromagnetically coupled S = 5/2 centers with g = 2.00. The magnetic susceptibility data were fit by using an expression derived from the spin-only isotropic HDvV exchange Hamiltonian $\mathcal{H} = -2J\mathbf{S}_1 \cdot \mathbf{S}_2$, where $\mathbf{S}_1 = \mathbf{S}_2 = 5/2$. The best fit was obtained for J = +0.69(4) cm^{−1} for **1c** (Figure 12) and J = +0.70(4) cm^{−1} for **2c** (Figure S6 of the Supporting Information) by fixing g = 2.00.

Compounds **1c** and **2c** belong to a rare class of diiron(III) clusters displaying ferromagnetic interactions. Other examples include [Fe₂(salmp)₂],³⁷ in which two phenoxide bridging ligands

(72) Lee, D.; Lippard, S. J. *J. Am. Chem. Soc.* **2001**, *123*, 4611–4612.

(73) Lee, D.; Hung, P.-L.; Spingler, B.; Lippard, S. J. *Inorg. Chem.* **2002**, *41*, 521–531.

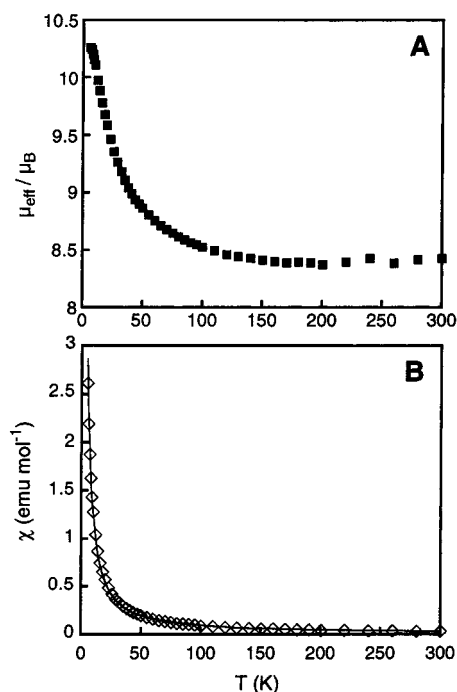


Figure 12. Plots of effective moment (μ_{eff}) per molecule versus temperature (A) and molar susceptibility (χ_M) versus temperature (B) for $[\text{Fe}_2(\mu\text{-OH})_2(\mu\text{-O}_2\text{CAr}^{\text{Tol}})_2(\text{O}_2\text{CAr}^{\text{Tol}})_2(\text{C}_5\text{H}_5\text{N})_2]$ (**1c**). The solid line in B corresponds to the best fit, obtained by parameters described in the text.

mediate weak ferromagnetic coupling ($J = +1.21 \text{ cm}^{-1}$) between two high-spin Fe(III) centers separated by $3.063(1) \text{ \AA}$ ($\text{Fe}-\text{O}_{\text{phenoxide}}-\text{Fe} = 97.06(9)^\circ$).⁷⁴ Structurally related di(μ -hydroxo)diiron(III) compounds, $[\text{L}_2\text{Fe}_2(\mu\text{-OH})_2]$ ³⁷ ($\text{Fe}\cdots\text{Fe} = 3.155(3) \text{ \AA}$; $\text{Fe}-\text{O}_{\text{hydroxide}}-\text{Fe} = 102.8(3)^\circ$) and $[(\text{dipic})\text{Fe}(\mu\text{-OH})_2(\text{H}_2\text{O})_2]$ ³⁷ ($\text{Fe}\cdots\text{Fe} = 3.089(2) \text{ \AA}$; $\text{Fe}-\text{O}_{\text{hydroxide}}-\text{Fe} = 103.6(2)^\circ$), however, display weak AF interactions with $J = -10.4$ and -11.4 cm^{-1} , respectively.^{68,69} The smaller $\text{Fe}-\text{O}_{\text{hydroxide}}-\text{Fe}$ angles in **1c** and **2c**, owing to the presence of two μ -1,3 carboxylate ligands, may lead to a crossover from antiferromagnetism to ferromagnetism.

Discussion

Spectroscopic Identification of Intermediates in the Reaction of $[\text{Fe}_2(\text{O}_2\text{CAr}^{\text{Tol}})_4\text{L}_2]$ Complexes with Dioxygen. Oxygenation of **1a** and **2a** in CH_2Cl_2 at -78°C generates thermally sensitive intermediates **1b** and **2b**, which decay to afford **1c** and **2c**, respectively, as the isolated products (Scheme 2). The electronic structures of **1b** and **2b** were probed by various spectroscopic techniques. EPR and Mössbauer studies provided compelling evidence that **2b** comprises equimolar amounts of $\text{Fe}^{\text{III}}\text{Fe}^{\text{IV}}$ and $\text{Fe}^{\text{II}}\text{Fe}^{\text{III}}$ as major components. Independent chemical synthesis and spectroscopic characterization of the $\text{Fe}^{\text{II}}\text{Fe}^{\text{III}}$ complexes, **1mv** and **2mv**,⁴⁰ enabled us to understand fully the contribution of each paramagnetic component to the overall spectroscopic properties of **1b** and **2b**.

The intense ($\epsilon = 1600\text{--}1700 \text{ M}^{-1} \text{ cm}^{-1}$, based on $[\text{Fe}_2]$) visible transitions at $660\text{--}670 \text{ nm}$ as well as the thermal instability of **1b** and **2b** are reminiscent of the properties of (peroxo)diiron(III) clusters. Peroxide-to-iron(III) LMCT transitions in these units usually occur at $500\text{--}800 \text{ nm}$ with extinction

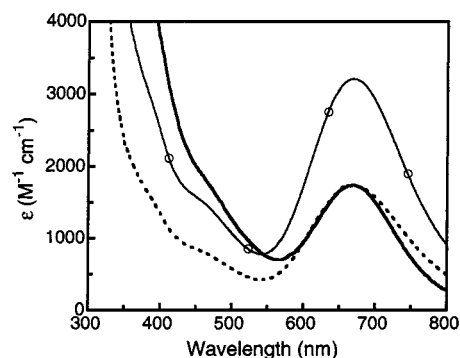


Figure 13. Comparison of the electronic absorption spectra of $[\text{Fe}_2(\mu\text{-O}_2\text{CAr}^{\text{Tol}})_4(4\text{-BuC}_5\text{H}_4\text{N})_2](\text{PF}_6)$ (**2mv**) (solid line with \circ) and **2b** (solid line) in CH_2Cl_2 . The dotted line represents the spectrum of **2mv** scaled to 54% to match the absorption maximum of **2b** at 670 nm.

coefficients exceeding $\sim 1000 \text{ M}^{-1} \text{ cm}^{-1}$ (Table S1), values significantly above those ($390\text{--}520 \text{ M}^{-1} \text{ cm}^{-1}$) of the $674\text{--}688 \text{ nm}$ absorption maxima displayed by valence-trapped $\text{Fe}^{\text{II}}\text{Fe}^{\text{III}}$ complexes $[\text{Fe}_2(\mu\text{-O})(\mu\text{-O}_2\text{CR})_2(\text{Me}_3\text{TACN})_2]^+$ ($\text{R} = \text{CH}_3$ or C_6H_5).^{37,75} No isotope-sensitive O–O vibrations, however, were detected in the resonance Raman spectra of **1b**. UV–vis data of **1mv** and **2mv**⁴⁰ now unambiguously establish that the optical transitions of **1b** and **2b** actually arise from the mixed-valence $\text{Fe}^{\text{II}}\text{Fe}^{\text{III}}$ components, $[\text{Fe}_2(\mu\text{-O}_2\text{CAr}^{\text{Tol}})_4(\text{C}_5\text{H}_5\text{N})_2]^+$ ($\lambda_{\text{max}} = 660 \text{ nm}$; $\epsilon = 2900 \text{ M}^{-1} \text{ cm}^{-1}$) and $[\text{Fe}_2(\mu\text{-O}_2\text{CAr}^{\text{Tol}})_4(4\text{-BuC}_5\text{H}_4\text{N})_2]^+$ ($\lambda_{\text{max}} = 670 \text{ nm}$; $\epsilon = 3200 \text{ M}^{-1} \text{ cm}^{-1}$), respectively. In Figure 13 are displayed the UV–vis spectra of **2b** and **2mv** scaled such that the absorption maxima match one another. The $\lambda_{\text{max}} = 670 \text{ nm}$ chromophore of **2b** is perfectly accounted for by the intervalence charge-transfer (IVCT) band of the $\text{Fe}^{\text{II}}\text{Fe}^{\text{III}}$ cation that constitutes $\sim 54\%$ of the total diiron concentration. This result is consistent with the ~ 0.45 oxidizing equivalent of **2b** determined by redox titration with Cp^*_2Fe . The mixed-valence species **2mv** ($\text{Fe}^{\text{II}}\text{Fe}^{\text{III}}/\text{Fe}^{\text{II}}\text{Fe}^{\text{II}} = +244 \text{ mV}$ vs SCE)⁷⁶ acts as a one-electron oxidant toward Cp^*_2Fe ($\text{Fe}^{\text{II}}/\text{Fe}^{\text{III}} = -130 \text{ mV}$ vs SCE)⁶⁴ to afford **2a** and Cp^*_2Fe^+ . A similar analysis can be made with **1b**, for which the corresponding **1mv** component has $\lambda_{\text{max}} \cong 665 \text{ nm}$. Comparison of the extinction coefficients indicates that **1b** comprises $\sim 55\%$ of **1mv**. Taken together, these results indicate that the dark green color of **1b** and **2b** arises predominantly from the $\text{Fe}^{\text{II}}\text{Fe}^{\text{III}}$, not the $\text{Fe}^{\text{III}}\text{Fe}^{\text{IV}}$, component in the oxygenation reaction mixture. For comparison, the $\text{Fe}^{\text{III}}\text{Fe}^{\text{IV}}$ chromophore in RNR–R2 X has an absorption band at $\sim 360 \text{ nm}$ and none at higher wavelengths.^{11b}

The resonance enhanced peak at 851 cm^{-1} in the Raman spectra of **1b** and **2b** originates from the $\text{Fe}^{\text{II}}\text{Fe}^{\text{III}}$ components **1mv** and **2mv**, respectively, and is thus not affected by ^{18}O labeling. At present, we do not have an assignment for this vibration, which is observed upon excitation of the IVCT band of the valence-delocalized $\text{Fe}^{\text{II}}\text{Fe}^{\text{III}}$ cores.

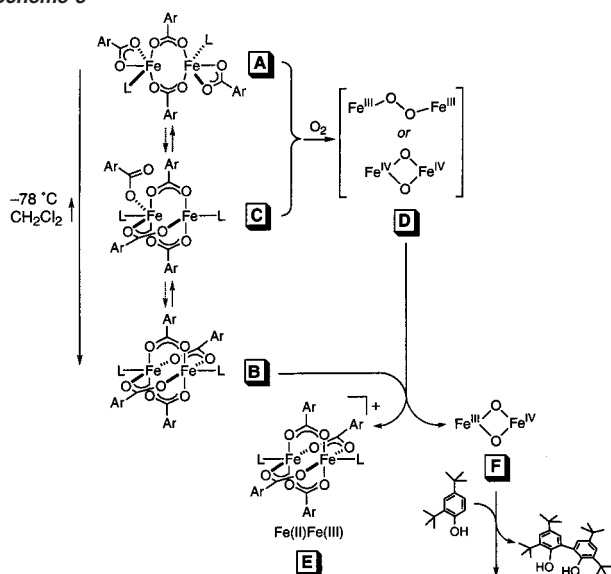
Mechanistic Considerations. Formation of $\text{Fe}^{\text{III}}\text{Fe}^{\text{IV}}$ and $\text{Fe}^{\text{II}}\text{Fe}^{\text{III}}$ species from a reaction between an $\text{Fe}^{\text{II}}\text{Fe}^{\text{II}}$ precursor and dioxygen is an unprecedented process among non-heme diiron systems. On the basis of the spectroscopic and kinetic data obtained here and in other investigations,^{35,40} we propose the working mechanism depicted in Scheme 3 to account for this novel chemical transformation.

(74) Snyder, B. S.; Patterson, G. S.; Abrahamson, A. J.; Holm, R. H. *J. Am. Chem. Soc.* **1989**, *111*, 5214–5223.

(75) Payne, S. C.; Hagen, K. S. *J. Am. Chem. Soc.* **2000**, *122*, 6399–6410.

(76) $\text{Fc}/\text{Fc}^+ = 0.46 \text{ V}$ vs SCE.; 0.40 V vs NHE.⁶⁴

Scheme 3



(a) Carboxylate Shifts. In the solution state, we presume an equilibrium between doubly bridged (**A**, Scheme 3) and quadruply bridged (**B**, Scheme 3) isomers of the $[\text{Fe}_2(\text{O}_2\text{CAr}^{\text{Tol}})_4\text{L}_2]$ module. This postulate reflects the fact that both **1a** and **2a** display essentially identical reactivity patterns toward dioxygen, affording reaction intermediates **1b** and **2b** having comparable spectral properties (vide supra). Given the distinctively different solid-state structures of **1a** (isomer **A**) and **2a** (isomer **B**), this result is quite unexpected. The steric environments of the coordinatively unsaturated metal centers in **A** and **B** are significantly different, as indicated by space-filling representations (Figure 14). Open coordination sites on the five-coordinate iron atoms in **A** are readily accessible to exogenous ligands, whereas the coordination sites available for the sixth ligand in **B** lies along the Fe–Fe vector buried inside the hydrophobic cavity. Core rearrangement is thus required for **B** before dioxygen binding.

Variable temperature ^{19}F NMR studies indicated that a related compound $[\text{Fe}_2(\text{O}_2\text{CAr}^{4-\text{FPh}})_4(\text{THF})_2]$ ³⁷ can exist in both isomeric forms **A** (windmill) and **B** (paddlewheel), the relative populations of which strongly depend on the temperature.⁷⁷ In CH_2Cl_2 at -80°C , **B** is a dominant isomer for $[\text{Fe}_2(\text{O}_2\text{CAr}^{4-\text{FPh}})_4(\text{THF})_2]$, although both **A** and **B** are present at room temperature. Such flexibility is illustrated by structural characterization of the mixed-valence $\text{Fe}^{\text{II}}\text{Fe}^{\text{III}}$ compounds $[\text{Fe}_2(\mu\text{-O}_2\text{CAr}^{\text{Tol}})_4\text{L}_2]\text{X}$ ($\text{L} = \text{THF}, \text{C}_5\text{H}_5\text{N}$; $\text{X}^- = \text{PF}_6^-, \text{OTf}^-$).⁴⁰ Here, a paddlewheel core forms following one-electron oxidation of a windmill core without any apparent steric penalty. These findings corroborate speculation that both isomeric forms, **A** and **B**, can be accessed by **1a** and **2a** under certain conditions. Formal double carboxylate shifts between $\mu\text{-1,3}$ bridging and η^2 -terminal positions would allow core interconversion between **A** and **B** to occur by a triply bridged intermediate **C**. We propose that the paddlewheel isomer **B** dominates the solution population of both **1a** and **2a** at low temperatures.

(b) Nature of the Initial O₂ Adduct(s). As mentioned above, core rearrangement in **B** is required to provide a dioxygen binding site. Shifts of one or two bridging carboxylate ligands in **B** would afford **C** or **A** as functionally competent isomers.

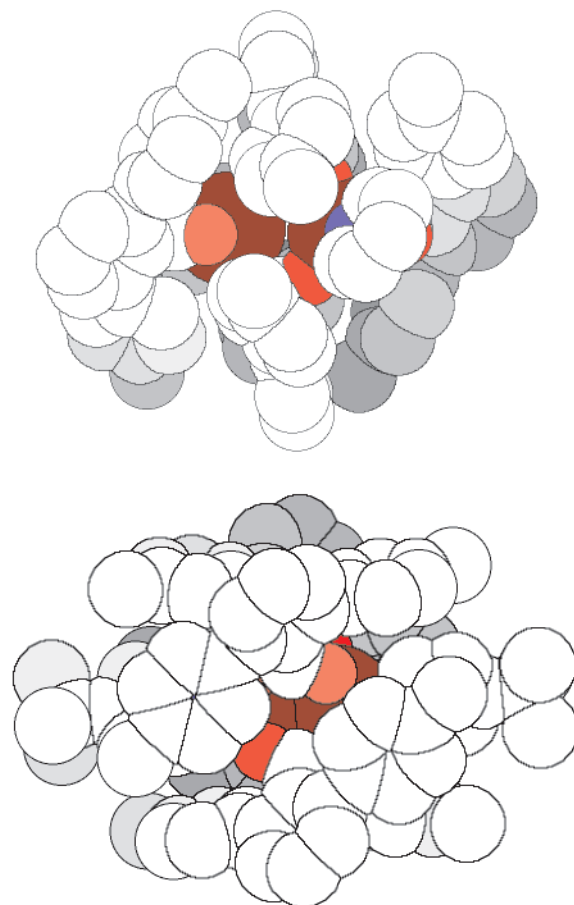
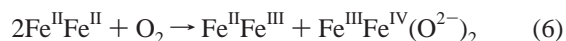


Figure 14. Space-filling representations of $[\text{Fe}_2(\mu\text{-O}_2\text{CAr}^{\text{Tol}})_2(\text{O}_2\text{CAr}^{\text{Tol}})_2(\text{C}_5\text{H}_5\text{N})_2]$ (**1a**) (top) and $[\text{Fe}_2(\mu\text{-O}_2\text{CAr}^{\text{Tol}})_4(4\text{-tBuC}_5\text{H}_4\text{N})_2]$ (**2a**) (bottom) generated using the crystallographic coordinates,^{34,35} where N is blue, O is bright red, and Fe is dark red.

Reaction of the diiron(II) species with dioxygen leads to an initial adduct **D**, which, by analogy to the RNR–R2 and MMOH intermediates,¹ is most likely either a peroxo-type $\{\text{Fe}^{\text{III}}_2(\text{O}_2^{2-})\}^{4+}$ or a Q-type $\{\text{Fe}^{\text{IV}}_2(\text{O}_2^{2-})\}^{4+}$ unit. Although rapid reaction with **B** (vide infra) precluded detailed investigation of **D** under the conditions employed, the sterically more hindered analogue of **1a**, $[\text{Fe}_2(\mu\text{-O}_2\text{CAr}^{\text{Mes}})_2(\text{O}_2\text{CAr}^{\text{Mes}})_2(\text{MeCN})_2]$,³⁷ reacts with dioxygen to afford a (peroxo)diiron(III) intermediate.²¹ A (peroxo)diiron(III) intermediate precedes the assembly of a $\{\text{Fe}^{\text{III}}\text{Fe}^{\text{IV}}(\text{O}^{2-})_2\}^{3+}$ core in reactions between $[\text{Fe}_2(\mu\text{-OH})_2(6\text{-Me}_3\text{TPA})_2]^{2+}$ and dioxygen.^{22,26,37}

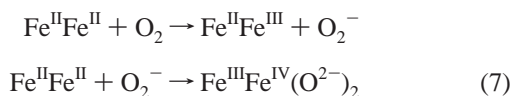
(c) Paramagnetic Intermediates. The first spectroscopically observable intermediates **1b** and **2b** contain equimolar amounts of $\text{Fe}^{\text{II}}\text{Fe}^{\text{III}}$ (**E**) and $\text{Fe}^{\text{III}}\text{Fe}^{\text{IV}}$ (**F**) species as major constituents (Scheme 3). The spectroscopic properties of **E** match perfectly those of **1mv** and **2mv**, indicating that **E** indeed is a one-electron oxidized form of **B**, $[\text{Fe}_2(\mu\text{-O}_2\text{CAr}^{\text{Tol}})_4\text{L}_2]^+$ ($\text{L} = \text{C}_5\text{H}_5\text{N}$ or $4\text{-tBuC}_5\text{H}_4\text{N}$). Formation of a 1:1 mixture of **E** and **F** requires formal four-electron oxidation of two molecules of $\text{Fe}^{\text{II}}\text{Fe}^{\text{II}}$ precursors. This metal oxidation is coupled to four-electron reduction of dioxygen, formally affording two oxo groups. Accordingly, **F** is formulated as $\text{Fe}^{\text{III}}\text{Fe}^{\text{IV}}(\text{O}^{2-})_2$ (eq 6).



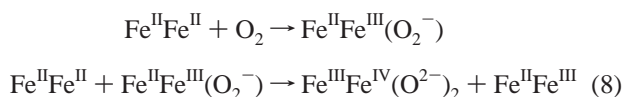
The nature of the oxidant effecting one-electron oxidation of **B** to **E** has significant implications about the chemistry we

(77) Lee, D.; Lippard, S. J. Submitted for publication.

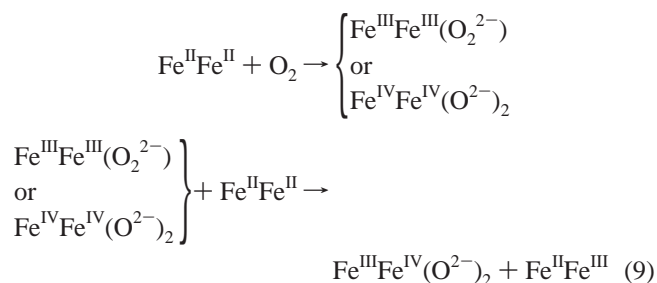
observe. Both dioxygen and a metal-based oxidant might promote outer-sphere electron transfer (ET), a process that would preserve the structural integrity of the $\text{Fe}^{\text{II}}\text{Fe}^{\text{II}}$ precursor. Outer-sphere ET from **B** to O_2 would generate **E** and a superoxide anion. Formal three-electron reduction of the latter by **B** would afford **F** (eq 7). The first step in this conversion has been



previously implicated in the formation of mixed-valence $\text{Fe}^{\text{II}}\text{Fe}^{\text{III}}$ compounds having at least one single atom bridging ligand.^{59,75,78,79} Considering the oxidation potential ($\text{Fe}^{\text{II}}\text{Fe}^{\text{II}}/\text{Fe}^{\text{II}}\text{Fe}^{\text{III}} = +284$ mV vs NHE)^{40,76} of **2a** in CH_2Cl_2 , however, we can rule out the outer-sphere, one-electron reduction of dioxygen ($\text{O}_2/\text{O}_2^- = -330$ mV vs NHE)⁸⁰ as a coupled process for the formation of **E**. Alternatively, inner-sphere ET from metal-bound O_2 might be invoked (eq 8). To account for the simultaneous formation of an equimolar quantity of **F**, however, the superoxide complex would have to be selectively and completely trapped by another equivalent of **B**, which seems unlikely. Moreover, there is no precedent for the three-electron reduction of superoxide by iron(II) compounds.



Instead, we propose that **D** acts as a one-electron oxidant toward **B**, affording the observed 1:1 mixture of **E** and **F** (eq 9). The coupled formation of **E** and **F** is fully consistent with the EPR kinetic data. Although rapid ET from **B** to **D** presumably prevents accumulation of a detectable amount of **D** under the conditions employed, the kinetic data provide compelling evidence for the presence of an intermediate preceding **E** and **F**, the most reasonable candidates being either a peroxo- or a Q-type dioxygen adduct.



(d) Oxidation of Phenol Substrates: Functional Mimic of RNR–R2, Species X. The high-valent $\text{Fe}^{\text{III}}\text{Fe}^{\text{IV}}$ species **F** effects oxidation of phenol substrates. The ~40% yield of the coupled biphenol product from 2,4-di-*tert*-butylphenol is close to the upper limit (50% based on diiron(II) precursor) of **F** in the proposed mechanism (Scheme 3; eq 6), and consistent with the quantitation afforded by EPR and Mössbauer spectroscopy. Control experiments with the $\text{Fe}^{\text{II}}\text{Fe}^{\text{III}}$ compound **2mv**, which

cannot oxidize the phenols, confirmed that the oxidizing power of **2b** originates from **F**, which acts both as a one-electron oxidant and a proton acceptor. This process closely parallels the mechanism of RNR–R2, in which a high-valent $\text{Fe}^{\text{III}}\text{Fe}^{\text{IV}}$ intermediate **X** oxidizes an adjacent tyrosine residue. Related $\{\text{Fe}^{\text{III}}\text{Fe}^{\text{IV}}(\mu\text{-O})_2\}^{3+}$ core fragments supported on polypyridyl ligands effect similar transformations.^{22,81}

(e) Reactivity and Magnetic Properties: Structural Implications for $\text{Fe}^{\text{III}}\text{Fe}^{\text{IV}}$. Different reactivity patterns of **E** and **F** toward H^+ indicate that **F** has ligand unit(s), the protonation of which alters magnetic coupling between the metal centers. Addition of 0.5 equiv of H^+ prior to oxygenation only slightly affected the amount of **E** generated, whereas a 10-fold decrease was observed for **F** as determined by EPR spectroscopy. Consistent with this finding, the contribution of **E** to the visible absorption of **1b** was not affected by addition of 2 equiv of H^+ at -78 °C. This result indicates that the structural integrity of the $[\text{Fe}_2(\text{O}_2\text{CAR}^{\text{Tot}})_4\text{L}_2]^+$ cation (**E**) is maintained in the presence of H^+ , whereas protonation of the putative O_2 -derived ligand(s) significantly decreases the stability of **F** as well as increasing its rate of reduction. The formulation of the **F** core as $\{\text{Fe}^{\text{III}}\text{Fe}^{\text{IV}}(\text{O}^{2-})_2\}^{3+}$ is compatible with such an observation. Protonation of the oxo groups in $\{\text{Fe}^{\text{III}}\text{Fe}^{\text{IV}}(\text{O}^{2-})_2\}^{3+}$ may trigger reduction of the Fe(IV) center to Fe(III), affording an $\text{Fe}^{\text{III}}\text{Fe}^{\text{III}}$ species. At this point, we cannot conclusively determine which species serves as an electron donor for **F**. Since the amount of **E** produced upon oxygenation is only slightly affected in the presence of H^+ , we believe that both **B** and **E** could act as reductants for **F**.

The large exchange coupling constant of $|2J| > 200$ cm^{-1} ($\mathcal{H} = -2J\mathbf{S}_1\cdot\mathbf{S}_2$), estimated for **F** by EPR spectroscopy,³⁵ implies the presence of an efficient superexchange pathway.^{1g} We propose that at least one of the oxo groups within the $\{\text{Fe}^{\text{III}}\text{Fe}^{\text{IV}}(\text{O}^{2-})_2\}^{3+}$ core in **F** acts as a bridging ligand, mediating the strong net AF interaction between the Fe(III) and Fe(IV) sites. A valence-localized $\text{Fe}^{\text{III}}\text{Fe}^{\text{IV}}$ complex having a $\{\text{Fe}_2(\mu\text{-O})_2\}^{3+}$ core also exhibits a large coupling, $|2J| > 80$ cm^{-1} ($\mathcal{H} = -2J\mathbf{S}_1\cdot\mathbf{S}_2$).^{32b} Although the correlation between *J* and the shortest Fe–O–Fe pathway has been well-established for (μ -oxo)diiron(III) complexes,⁸² an analogous magnetostructural correlation is not available for the $\text{Fe}^{\text{III}}\text{Fe}^{\text{IV}}$ units, largely owing to the limited number of well-defined basis sets available.

(f) Decay of the Intermediates and Isolation of a Diiron(III) Complex. Mechanistic information about the decomposition of **E** and **F** is currently unavailable. Studies of **1mv** and **2mv** reveal that **E** is thermally stable but rapidly decomposes in the presence of dioxygen at room temperature.⁴⁰ Decomposition of **E** upon warming thus can be partially ascribed to reactions with residual dioxygen. Alternatively, reactions between **E** and **F** may occur at elevated temperatures, although preliminary EPR data suggest that their decay processes are not coupled.

The EPR spectra obtained for a thermal decay product of **2b** (Figure 3) display spectral patterns distinctively different from that of **2c**. This result clearly indicates that **2c** is not an immediate reaction product of **2b**. Although the $\{\text{Fe}_2(\mu\text{-OH})_2\}^{4+}$ cores in **1c** or **2c** are reminiscent of analogous $\{\text{Cu}_2(\mu\text{-OH})_2\}^{2+}$ cores obtained following C–H activation by high-valent $\{\text{Cu}_2-$

(78) Bossek, U.; Hummel, H.; Weyhermüller, T.; Bill, E.; Wieghardt, K. *Angew. Chem., Int. Ed. Engl.* **1995**, *34*, 2642–2645.

(79) Cohen, J. D.; Payne, S.; Hagen, K. S.; Sanders-Loehr, J. *J. Am. Chem. Soc.* **1997**, *119*, 2960–2961.

(80) Bertini, I.; Gray, H. B.; Lippard, S. J.; Valentine, J. S. *Bioinorganic Chemistry*; University Science Books: Mill Valley, CA, 1994.

(81) Kim, C.; Dong, Y.; Que, L., Jr. *J. Am. Chem. Soc.* **1997**, *119*, 3635–3636.

(82) Gorun, S. M.; Lippard, S. J. *Inorg. Chem.* **1991**, *30*, 1625–1630.

(μ -O)₂}²⁺ intermediates,⁴¹ no ligand oxidation was observed in the present investigation. The good to excellent isolated yields (75–90%) of **1c** and **2c** also strongly suggest that not all of the oxygen atoms in the OH[−] bridging ligands originate from O₂. Incorporation of adventitious H₂O in the crystallization media most likely contribute to the assembly of the {Fe₂(μ -OH)₂}⁴⁺ core from the initial thermal decay product(s), the details of which were not further investigated.

(g) Branching Pathways. In addition to the major intermediates **E** and **F** described above, a diiron(III) component was detected in EPR and Mössbauer samples of **2b**.³⁵ Although the mechanism depicted in Scheme 3 does not account for the formation of this diiron(III) product, it must arise either through a reaction between **E** and **F** or via a branching pathway involving the diiron(II) precursor and dioxygen. Such processes could be operative in the concentrated (>10 mM) diiron solutions used for the manometry, EPR, and Mössbauer studies. The stoichiometry of O₂ consumption (0.75 ± 0.1 equiv per diiron(II)) exceeds that (0.50) expected solely from the chemistry of eq 6, implying the involvement of additional, unidentified oxygenation processes. Thermal decay or reactions with **E** may be responsible for the detection of less than a quantitative amount of **F** in the Mössbauer sample, which required solvent removal at −78 °C over a period of >18 h to prepare.

Biomimetic Formation of Fe^{III}Fe^{IV} Species: Relevance to RNR–R2. A high-valent Fe^{III}Fe^{IV} species has now been prepared by reaction of dioxygen with [Fe₂(O₂CR)₄L₂] diiron(II) complexes, a process that closely mimics the formation of the enzyme intermediate RNR–R2 X (Scheme 1). Prior to our previous communication of this chemistry,³⁵ no synthetic system existed that utilized dioxygen as a terminal oxidant to access the Fe(IV) state from Fe(II) precursors. Analogous high-valent non-heme Fe^{III}Fe^{IV} compounds had previously been obtained only by oxidation of di(μ -oxo)diiron(III) precursors with H₂O₂,³² and in these cases polypyridyl ligands unlike those in the proteins were employed.

One external electron is required to balance the equation for the formation of a tyrosyl radical and the (μ -oxo)diiron(III) core describing the reaction between reduced RNR–R2 and O₂ (Scheme 1). The source of this extra electron and its injection point along the reaction coordinate are currently unclear. After our communication of this RNR–R2 model chemistry,³⁵ another synthetic system was reported, in which a polypyridine-supported diiron(II) center reacts with dioxygen to afford a (peroxo)diiron(III) species.^{22,26} In the presence of 1 equiv of H⁺, this intermediate transformed into an Fe^{III}Fe^{IV} complex, and again the source of the extra electron needed for the conversion of the former to the latter was not established. A recent mechanistic proposal suggests that, in RNR–R2, the diiron clusters are functionally distinctive, one reacting with dioxygen and the other supplying reducing equivalents.⁸³ Although the requisite Fe^{II}Fe^{III} intermediate has yet to be identified in the biological system, the mechanism depicted in Scheme 3 suggests that carboxylate-bridged diiron(II) centers can indeed function to supply the required electron by ET. It still remains to be determined, however, whether the ET occurs directly to a (peroxo)diiron(III) unit or whether conversion to a

Q-type transient intermediate is involved that accepts the electron to afford the Fe^{III}Fe^{IV} intermediate X.

Self-hydroxylating monooxygenase reactivities occur in certain mutants of RNR–R2,⁸⁴ which strongly support a unifying theory connecting the chemistry of non-heme dioxygen-activating centers. A similar one-electron reduction of the high-valent diiron(IV) species in MMOHQ could be effectively blocked either by the lack of an efficient ET pathway or by the binding of other MMO component proteins. Conformational changes in the primary metal coordination sphere might be induced by such binding events, which could shift the redox window to avoid deleterious quenching of the oxidizing equivalents.

Summary and Perspective

Tetracarboxylate diiron(II) complexes react with dioxygen to access the Fe(IV) oxidation state, a process that parallels the chemistry of several non-heme diiron enzymes. The spectroscopic and functional properties of the Fe^{III}Fe^{IV} species faithfully reproduce features of the enzyme intermediate RNR–R2 X. Spectroscopic and kinetic studies revealed the simultaneous formation of both Fe^{II}Fe^{III} and Fe^{III}Fe^{IV} species in this transformation, the mechanistic implications of which relate well to a recent proposal for the enzyme. The untimely ET from the low-valent starting material to putative high-valent dioxygen adduct(s), as proposed in this investigation, poses a significant challenge for future work to access dioxygen-activating model compounds that functionalize hydrocarbons. Bulky ligand fragments have been frequently exploited to shield highly reactive species against unwanted side reactions. Although the steric hindrance provided by such constructs may suppress reactions involving bond-forming processes, deleterious ET reactions may still occur even between well-shielded small molecules. Uncontrolled electron trafficking may quench a reactive intermediate before it accumulates in amounts sufficient to effect the chemical transformations of interest. A detailed understanding of this process would undoubtedly facilitate efforts to gain better control over the oxidizing power of dioxygen in synthetic constructs.

Acknowledgment. This work was supported by grants from the National Science Foundation and National Institute of General Medical Sciences. We thank Drs. J. Du Bois and T. J. Mizoguchi for many helpful discussions, Dr. A. M. Barrios and Ms. J. Bautista for performing the resonance Raman experiments, and Ms. J. Kuzelka for assistance in acquiring the Mössbauer spectra.

Supporting Information Available: Physical characterization of **1mv**, **2b**, **2mv**, and **2c** (Figures S1–S4, S6), an ORTEP diagram of [Fe(O₂CAr^{Tol})₂(2,4-^tBu₂C₆H₃O)(4-^tBuC₅H₄N)] (Figure S5), and an X-ray crystallographic file (CIF, PDF). This material is available free of charge via the Internet at <http://pubs.acs.org>.

JA012251T

(83) Miller, M. A.; Gobena, F. T.; Kauffmann, K.; Münck, E.; Que, L., Jr.; Stankovich, M. T. *J. Am. Chem. Soc.* **1999**, *121*, 1096–1097.

(84) (a) Örmö, M.; deMaré, F.; Regnström, K.; Åberg, A.; Sahlin, M.; Ling, J.; Loehr, T. M.; Sanders-Loehr, J.; Sjöberg, B.-M. *J. Biol. Chem.* **1992**, *267*, 8711–8714. (b) Åberg, A.; Örmö, M.; Nordlund, P.; Sjöberg, B.-M. *Biochemistry* **1993**, *32*, 9845–9850. (c) Örmö, M.; Regnström, K.; Wang, Z.; Que, L., Jr.; Sahlin, M.; Sjöberg, B.-M. *J. Biol. Chem.* **1995**, *270*, 6570–6576. (d) Baldwin, J.; Voegtli, W. C.; Khidekel, N.; Moënné-Loccoz, P.; Krebs, C.; Pereira, A. S.; Ley, B. A.; Huynh, B. H.; Loehr, T. M.; Riggs-Gelasco, P. J.; Rosenzweig, A. C.; Bollinger, J. M., Jr. *J. Am. Chem. Soc.* **2001**, *123*, 7017–7030.